LAYER-BY-LAYER ASSEMBLY OF TWO-DIMENSIONAL TITANIUM CARBIDE MXENE BASED PH SENSORS

A Thesis

by

IAN JOHNNY ECHOLS

Submitted to the Office of Graduate and Professional Studies of
Texas A&M University
in partial fulfillment of the requirements for the degree of

MASTER OF SCIENCE

Chair of Committee,	Jodie L. Lutkenhaus
Committee Members,	Micah J. Green
	Miladin Radovic
	Zhengdong Cheng
Head of Department,	Arul Jayaraman

December 2019

Major Subject: Chemical Engineering

ABSTRACT

pH sensors are widely used to monitor chemical reactions, environmental conditions, and physiological pH due to the importance of alkalinity/acidity in these applications. Currently, the most widely used techniques for measuring pH are glass electrodes and single use pH strips. However, both methods have their limitations (e.g. portability and fragility for glass electrodes, limited reuse and poor sensitivity of pH strips). Herein, we use layer-by-layer (LbL) electrostatic self-assembly to fabricate a flexible and highly sensitive titanium carbide ($Ti_3C_2T_x$) MXene based pH sensor. $Ti_3C_2T_x$ is the most common MXene to date and has drawn considerable attention due to its high conductivity and functionalized surface. By combining $Ti_3C_2T_x$ with a positively charged polymer via LbL assembly, we successfully fabricate nanometer scale thin films. As the sensor is exposed to environments of varying pH, the hydroxyl surface groups of the $Ti_3C_2T_x$ (de)protonate as H_3O^+ and OH^- ions interact with the surface. This leads to a change in electrostatic attraction between nanosheets and a reduction in the number of active sites. When this occurs, the resistance of the sensors changes, allowing for use of the materials as a resistive pH sensor. With the inclusion of a pH sensitive polymer, such as BPEI, we show the ability to enhance sensitivity of the sensor due to the conformational changes of BPEI due to (de)protonation with changes in pH. This work discusses the use of $Ti_3C_2T_x$ in a highly sensitive, flexible pH sensor and creates prospects in the field of wearable and portable sensors.

CONTRIBUTORS AND FUNDING SOURCES

Contributors

Thesis committee members included Professor Jodie Lutkenhaus, Professor Micah Green, and Professor Zhengdong Cheng from the Chemical Engineering (CHEN) Department and Professor Miladin Radovic from the Material Science and Engineering (MSEN) Department.

Zeyi Tan and Evan Prehn from Professor Miladin Radovic's group in the MSEN Department prepared MAX phase powders and etched MAX phase powders into $Ti_3C_2T_x$ clay and obtained XRD data for the MAX phase powders. Xiaofei Zhao from Professor Micah Green's group in the CHEN Department processed $Ti_3C_2T_x$ clay into $Ti_3C_2T_x$ nanosheets and obtained SEM and AFM data for the starting nanomaterials and XRD data for the $Ti_3C_2T_x$ nanosheets. Dr. Touseef Habib and Dr. Smit Shah assisted with synthesis of $Ti_3C_2T_x$ nanosheets. Dr. Wanmei Sun from Professor Micah Green's group synthesized graphene oxide dispersions. SEM, AFM, and XPS instruments were provided by the TAMU Materials and Characterization Facility. Use of the TAMU Materials and Characterization Facility and assistance of Dr. Yordanos Bisrat and Dr. Jing Wu are acknowledged. The Soft Matter Facility at Texas A&M provided the Zetasizer. XRD instruments were provided by the TAMU Chemistry Department.

Funding Sources

This work was supported by the US National Science Foundation (NSF) under award number 1760859.

NOMENCLATURE

A	area between electrodes (cm^2) or absorbance (a.u.)
AA	ascorbic acid
a.u.	absorbance units or arbitrary units
AFM	atomic force microscopy
Al	aluminum
AWG	American wire gauge
BPEI	branched polyethylenimine
C	coulomb
c	concentration (M)
DFT	density functional theory
DI	deionized
DC	direct current
DLS	dynamic light scattering
DMSO	dimethyl sulfoxide
E	potential difference across the glass membrane
E^o	standard cell potential
F	Faraday's constant (96,485 C/mol)
FET	field effect transistor
f_o	resonant frequency (Hz)
FWHM	full width half maximum
GO	graphene oxide

H_2	hydrogen
H_2O	hydrogen dioxide
HCl	hydrochloric acid
HER	hydrogen evolution reaction
HF	hydrofluoric acid
HI	hydroiodic acid
H_2O_2	hydrogen peroxide
H_2SO_4	sulfuric acid
I	intensity
I_o	initial intensity
K	Kelvin
K	extinction coefficient
$KMnO_4$	potassium permanganate
KOH	potassium hydroxide
l	path length (cm)
LbL	layer-by-layer
LiF	lithium fluoride
LP	layer pair
M	molar
N	refractive index
n	valence of the electron
$NaNO_3$	sodium nitrate

NaOH	sodium hydroxide
NH_3	ammonia
NH_4^+	ammonium
NH_4F_2	ammonium bifluoride
NIR	near infrared
PDADMA	poly (diallyldimethylammonium)
PDADMAC	poly (diallyldimethylammonium chloride)
PECS	Pulsed Electric Current System
PET	polyethylene terephthalate
PTFE	polytetrafluoroethylene
PVDF	polyvinyl difluoride
QCM	Quartz Crystal Microbalance
QD	quantum dot
R	resistance or gas constant (8.314 J/mol/K)
R_q	root mean square roughness
RDF	radial distribution function
rGO	reduced graphene oxide
RMS	root mean square
SEM	surface electron microscopy
T	temperature (K)
t	thickness (nm)
Ti	titanium

Ti_3AlC_2	titanium aluminum carbide
TiC	titanium carbide
TiCl	titanium chloride
$Ti_3C_2T_x$	titanium carbide MXene
TiO_2	titanium dioxide
TiOH	titanium hydroxide
UV	ultraviolet
VIS	visible
w	path width
XPS	x-ray photoelectron spectroscopy
XRD	x-ray diffraction
Δf	change in frequency
Δm	change in mass
ε	molar extinction coefficient (M^{-1} cm^{-1})
ρ	resistivity
ρ_q	density of quartz (2.68 g/cm^3)
μ_q	shear modulus of quartz crystal (2.95E11 g/cm/s^2)

TABLE OF CONTENTS

Page

LIST OF FIGURES

Page

LIST OF TABLES

Page

1. INTRODUCTION

1.1. MXenes

1.1.1. Discovery and Synthesis

MXenes were first discovered in 2011 at Drexel University.[1] MXenes are synthesized by the selective etching of the 'A' phase from a MAX phase material. The MAX phase material is composed of a transition metal, M, a group 13 or 14 transition metal, A, and either carbon or nitrogen, X.[1-4] Due to the lower bonding energy of the 'A' phase to 'M' and 'X', it is possible to selectively etch the 'A' phase out of the MAX phase material and obtain $M_{n+1}X_nT_x$ where T is a surface functional group, -OH, -O, or -F, and x is the number of functional groups. Initially, this was achieved by using hydrofluoric acid (HF) to etch Ti_3AlC_2 to $Ti_3C_2T_x$.[1] The resulting MXene possesses an 'accordion' like structure and can be readily delaminated to obtain MXene nanosheets with high conductivity. Due to the remaining 'M' and 'X' constituents after etching and the graphenic like structure, the resulting $M_{n+1}X_n$ was termed MXene.[5] However, concerns with the safety of using highly concentrated HF and possible over etching of the MAX phase material have led to the use of etchants that contain or react to form HF, such as lithium fluoride (LiF) and hydrochloric acid (HCl) as etchants, at least in the case of titanium based MXenes.[5-8] The reactions associated with HF based etching for the generic MXene, $M_{n+1}AlX_n$, are as follows[4,9,10]:

$$M_{n+1}AlX_n + 3HF = AlF_3 + 1.5H_2 + M_{n+1}X_n \quad (1)$$

$$M_{n+1}X_n + 2H_2O = M_{n+1}X_n(OH)_2 + H_2 \quad (2)$$

$$M_{n+1}X_n + 2HF = M_{n+1}X_nF_2 + H_2 \quad (3)$$

Reaction (1) is responsible for the etching of Al from the MAX phase material while reactions (2) and (3) are responsible for functionalizing the surface with -OH and -F, respectively. By controlling etching conditions, it is possible to control the distribution of functional groups which allows for tailoring use of the MXenes in downstream applications. For example, a lower HF concentration would lead to reaction (3) being limited and a decrease in the abundance of -F functional groups on the MXene.

Another means of controlling properties is by changing the etchant used. For example, Halim *et al.* demonstrated the use of ammonium bifluoride, NH_4F_2, in etching Ti_3AlC_2 and intercalating ammonia (NH_3) into the sheets of the resulting MXene.**[10]** Due to its surface functional groups, the surface of $Ti_3C_2T_x$ is negatively charged. This makes readily possible the intercalation of positively charged ions such as ammonium (NH_4^+) to maintain charge balance. The reactions for the NH_4F_2 based etching of Ti_3AlC_2 are[10]:

$$Ti_3AlC_2 + 3NH_4HF_2 = (NH_4)_3AlF_6 + Ti_3C_2 + 1.5H_2 \quad (4)$$

$$Ti_3C_2 + aNH_4HF_2 + bH_2O = (NH_3)_c(NH_4)_dTi_3C_2(OH)_xF_y \quad (5)$$

The intercalation of the NH_3 and NH_4^+ into the MXene sheets presents an additional means to control the properties of the MXene and has been explored by using a variety of cations.[11,12] The ability to tailor the properties of MXenes has generated promise in its use

for electrochemical energy storage as well as other applications.[13-16] Additionally, the intercalation of ions and adsorption of molecules onto the charged MXene surface shows potential for use of MXenes in catalysis and sensing. As the first discovered and most common MXene to date, $Ti_3C_2T_x$ has been the most studied MXene and will be the focus herein.

The mechanism of conductivity for $Ti_3C_2T_x$ was explained by Halim.[1,17,18] Ti_3AlC_2 has two sub-bands below the Fermi energy. The higher energy sub-band is attributed to the hybridization of Ti 3d and Al 3p orbitals whereas the lower energy sub-band is attributed to the hybridization of Ti 3d and C 2p orbitals.[18] When Al is removed during etching, the higher energy band gap is then composed of Ti 3d orbitals, leading to metallic Ti-Ti bonding. This results in $Ti_3C_2T_x$ exhibiting metallic conductivity.

Halim and Xie *et al*. also explored the effect of surface functional groups on conductivity.[17,18] The introduction of surface functional groups during etching leads to the formation of a third, lower energy, sub-band. This sub-band is attributed to the formation of Ti-T_x bonds and results in the two higher sub-bands to shift to lower energies.[17] This results in lower conductivities of $Ti_3C_2T_x$ and shows the importance of synthesis method on controlling properties. The reduction in conductivity due to surface groups is supported by the findings of Hart *et al*.[19] By annealing MXenes to remove surface functional groups, Hart *et al.* was able to increase the conductivity of the MXenes which is in line with the theoretical results of Xie *et al*.[17,19]

1.1.2. Safety Concerns

MXene synthesis poses several safety concerns.[6] The etching reaction is highly exothermic which makes scaling up difficult and the widespread use of HF as an etchant creates the potential for hazardous chemical exposure. Additionally, there is a risk of HF not being entirely washed out during post processing of the MXenes which would result in HF present during downstream applications. Even the synthesis of the parent MAX powders poses a safety hazard due to the flammability of the fine powders during sintering and tube furnacing.

Concerns with the high concentration of HF during etching have led to a push for other possible etchants as discussed previously. More recently, reaction conditions have been moving towards lower temperature regions and concentrations such as the minimally intensive layer delamination (MILD) method and fluoride free etching.[20,21]

1.1.3. Uses

Due to their high conductivity (~240,000 S/m for $Ti_3C_2T_x$), high surface to volume ratio, and functionalized surface, MXenes have drawn considerable interest in a variety of applications.[22] The major fields where MXenes pose a promising material include energy storage, adsorption, catalysis, and sensing.

1.1.3.1. Energy Storage

As Li^+ can easily intercalate in-between MXene sheets, MXenes have drawn considerable interest for use as energy storage devices since their inception.[23] Despite the

short time MXenes have been studied, various attempts to improve performance have already been explored including annealing MXenes to improve electrical properties and intercalation of various cations to improve capacitance.[13,24] Recently, use of MXene composites has also been explored to improve mechanical properties by improving stretchability in the case of Chang *et al.* and flexibility for Ling *et al*.[22,25,26] The ease of ion intercalation that enables use of MXenes as energy storage devices and the ability to improve mechanical properties through use of composites creates promise for use of MXenes in other applications.

1.1.3.2. Adsorption and Catalysis

Given the high surface area to volume ratios of two-dimensional materials, they are often ideal materials for adsorption. This holds especially true for MXenes as they also possess an abundance of surface groups: most notably hydroxyl (-OH) surface groups which facilitate hydrogen bonding. For example, Wang *et al.* demonstrated the use of V_2CT_x for uranium capture both theoretically and experimentally.[27] Uranium is able to adsorb to the abundant hydroxyl groups by an ion-exchange mechanism. This was supported by Zhang *et al.* with first principles simulation.[28] Li *et al.* demonstrated the capability of LbL assembly to improve adsorption due to the hierarchical structure obtained using this assembly method.[29] This structure allows for access to more adsorption sites and a mesoporous structure that facilitates diffusion which presents promise for continued use of MXenes in adsorption processes, particularly those related to sensing.

Catalysis is a promising application due to the high surface area to volume ratio and active surface sites for adsorption. One such use is for the hydrogen evolution reaction (HER).[30-32] This is possible due to the near ideal Gibbs free energy (0 eV) of adsorption of a hydrogen ion to oxygen terminated surface groups as supported by DFT. Recently, use of MXenes for the oxygen evolution reaction has been explored as well.[33,34]

1.1.3.3. Sensors

Due to their functionalized surface and high conductivity, MXenes have become a promising material for use in sensors. Their use as sensors have been demonstrated both in first principles studies, such as density functional theory (DFT), and experimentally.[35-38] DFT has been used to prove possible analytes for future MXene sensors. Typically, DFT will be used to determine adsorption energy of the analytes to the MXene sheets. These results can then be verified experimentally. However, due to the effect of surface groups on MXene properties, there can be some variation between simulation and experimental results.

To date, MXenes have been used as optical, resistive, amperometric, and potentiometric sensors for a variety of applications.[39-45] In the case of optical sensors, target ions interact with the surface of the MXene and fluorescent quenching occurs.[44,45] The concentration of the target ion can be determined based off the degree of quenching that occurs. Resistive, amperometric, and potentiometric sensors all rely on changes in electrical or electrochemical properties of the sensor. In the case of a sensor that displays Ohmic behavior, these all become interchangeable following Ohm's Law.

Resistive sensors and chemo resistors rely on changes in resistance of the sensor. This is often caused by changes in charge carrier mobility and/or conductive pathways. On the other hand, potentiometric and amperometric sensors behave similarly to one another. When molecules adsorb to the MXene surface groups, there are less available sites for charge carriers to travel through, resulting in a decrease of resistance. These sensor types are explained in more detail in future sections.

1.1.4. Oxidation

MXenes are extremely prone to oxidizing into their metal oxide when exposed to water or air. Habib *et al.* demonstrated effect of this oxidation on the electrical properties of MXenes.[46] The oxidation of the MXene to its metal oxide form leads to order of magnitude reductions in conductivity of the material. This poses issues in long term usage of MXenes in any applications that rely on its electrical properties such as energy storage and sensing. Lotfi *et al.* has also published on the effects of oxidation on the number of Ti-C, C-C, and Ti-O bonds as measured by radial distribution functions (RDFs).[47] The reduction in bond number of Ti-C is indicative of the degradation of the MXene. The results of their simulations also demonstrated the effect of temperature and environment on oxidation. Zhang *et al.* experimentally verified the reduction in MXene concentration over time as oxidation occurs and fit a model to his proposed reaction.[48] Zhang *et al.* proposed a water-induced oxidation or hydrolysis reaction as shown in Eq. 6.

$$Ti_3C_2O_2 + 4H_2O = 3TiO_2 + 2C + 4H_2 \quad (6)$$

As oxidation occurs, more MXene is converted to metal oxide and its favorable properties are undone.

However, there have been recent advances towards mitigating the effects of oxidation. Various groups have explored controlling the storage environment of MXenes to prevent oxidation. Zhang *et al.* used reduced temperatures and Argon (Ar) to mitigate oxidation and extend shelf life of MXenes on the order of days.[48] Habib *et al.* also investigated the use of reduced temperatures to mitigate oxidation by storing the MXenes in ice.[46] Additionally, Habib *et al.* used various aqueous media and polymer matrices to prevent oxidation.

More recently, VahidMohammadi *et al.* and Han *et al.* have explored using ions to 'protect' the MXene sheets from being oxidized.[11,12] In the case of VahidMohammadi *et al.*, alkali cations were added to a delaminated vanadium carbide MXene (V_2CT_x) solution. Due to the positive charge of the ions, they readily intercalated into the MXene nanosheets as proven by shifts in XRD peaks. VahidMohammadi *et al.* attributed the inhibition of oxidation to the decrease in charge density after ion insertion and verified stability of the treated vanadium carbide MXene with both XPS and XRD. Han *et al.* added an antioxidant, ascorbic acid (AA) in excess in order to prevent oxidation of the MXene.[12] In their case, stability was verified by spectrophotometry as they observed only a slight decrease in absorbance over time. Recently, NaAsc has been used to achieve this oxidation protection as well and the efficacy was verified by conductivity, hydrodynamic diameter, zeta potential, XPS, XRD, and DFT simulations.[49] The reducing properties of

the NaAsc mitigates oxidation of the MXene. Herein, we use a polymer composite and NaAsc to prevent oxidation as suggested by Habib *et al.* and Zhao *et al*.[46,49]

1.1.5. Behavior in Different pH Regimes

Due to the charged functional groups on the surface of MXenes and the charged edges of the nanosheets, MXenes are susceptible to changes in pH. Natu *et al.* reported on the crumpling of $Ti_3C_2T_x$ in both acidic and basic pH as well as the effect of pH on both zeta potential and hydrodynamic size.[50,51] In the latter work, Natu *et al.* demonstrated a linear relationship between zeta potential and pH in the acidic regime (pH 2 – pH 7), indicating a pH dependence of the MXene.[50] Zhao *et al.* also reported on the alkali induced crumpling of $Ti_3C_2T_x$.[52] While the surface of the nanosheets are negatively charged, the edges are positively charged at low pH (pH ~ 3). As pH continues to decrease, the electrostatic interaction between sheet surfaces and edges increases and leads to flocculation of the nanosheets.[50] On the other hand, at high pH, cations intercalate into the nanosheets, and the edges reach a neutral charge and sheet interaction mainly takes place at the negatively charged surface which also leads to aggregation.[50] The varying behavior of MXenes in different pH regimes and readily (de)protonated hydroxyl surface groups lead to the belief that MXenes can be used in pH responsive devices.

1.1.6. Ion Intercalation

As demonstrated by the use of MXenes for energy storage devices, ion intercalation readily occurs in between MXene sheets. The ion used for intercalation can

have a significant effect on the properties of the MXene. Wei *et al.* used a variety of alkaline solutions to tune the interlayer spacing of $Ti_3C_2T_x$.[53] Due to varying ionic radii of the cations used, different interlayer spacings, ranging from 0.45 nm in the case of KOH to 0.6 nm in the case of LiOH, were obtainable. The effect of different intercalant cations on adsorption was explored in their work to demonstrate the tunable properties of MXenes. The proclivity of ions to intercalate in-between MXene multilayers and the varying effects of different ions and ion concentrations makes MXenes a promising material for use in sensors.

1.2. Sensors

1.2.1. Uses of Sensors

Sensors have importance in a variety of applications including industrial, medical, and personal care. Each of these applications places a different set of requirements on the sensor type and due to the wide array of applications and subsequently conditions that sensors will be subjected to, it is necessary to have different types of sensors readily available.

1.2.2. Types of Sensors

Recently, there have been advances in a variety of types of sensors including potentiometric, amperometric, optical, and resistive.[39,54-57] Each type has its advantages and disadvantages (e.g. fragility, ease of use, sensitivity, response time, etc.) that determine what type of application the sensor is most suited for and leads to the need of

novel sensors to satisfy the requirements associated with recent technological advancements.

1.2.2.1. Potentiometric/Amperometric

Potentiometric and amperometric sensors are two prevalent types of novel sensors. While both rely on changes to electrical/electrochemical properties, the key difference between the two is the former measures voltage at a constant current, and the latter measures current at a constant voltage. In the case of an Ohmic sensor (linear I-V curve), these values are directly correlated. Due to the similarities, these sensor types will be discussed jointly.

Both of these sensor types typically rely on adsorption or intercalation of target molecules. When either of these phenomena occur, the number of available sites for charge transport is reduced, leading to a reduction in current in the case of amperometric sensors and voltage in the case of potentiometric sensors.[41,57] These sensor types have been used for a variety of analytes including biomolecules, pH, and gases.[41,56-58] While the response of potentiometric sensors is typically limited by the Nernstian limit (59.16 mV/pH), some exceptions occur.[59]

1.2.2.2. Optical

Optical sensors rely on a color change to display response such as colorimetric pH strips.[60] While this makes optical sensors simple to use, it means they also lack an accurate response without the aid of photometric analysis to quantify their results. Despite the lack

of precise responses, this sensor type is still favorable when only the pH range is needed. As such, there have been more recent developments in this sensor type that rely on quantum dots (QD).[39,61] Due to their small size, QDs exhibit excellent photoluminescent properties that allow for use in optical sensors and demonstrate future use in nano and intracellular sensors.

1.2.2.3. Resistive

Resistive sensors rely on a change in resistance to sense stimuli. However, they tend to have poor reversibility due to the chemical changes required for the resistance change.[62] Materials of construction for resistive sensors need to be highly conductive and have a functionalized surface group.[36] The high conductivity is necessary to mitigate noise and provide a higher resolution response. The functionalized surface group is needed to provide a surface for the analyte to respond to and generate a change in resistance.

Currently, resistive sensors are used for a variety of applications including strain and chemical sensing.[63] In the case of the former, the sensing mechanism relies on the physical deformation of the sensors. For example, An *et al.* demonstrated that the formation of cracks when the sensor was stretched led to an increase in resistance, allowing for highly sensitive strain detection.[64] The importance of the formation of microcracks for sensing was supported by Cai *et al.*[65] Resistive sensors have also been used to detect volatile organic compounds (VOCs).[36,66-68] These sensors operate on the adsorption of the analyte molecule to functional groups on the sensor or intercalation of the analyte molecule into the device. This allows for an increase in resistance associated

with increasing concentration of the target molecule. Resistive sensors have been applied as humidity sensors as well.[40] In the case of An *et al.*, MXene based sensors were used to detect relative humidity of the environment. Water molecules intercalated into the sensor, leading to increased thickness and subsequently resistance. This response mechanism is similar to that for MXenes in energy storage with water molecules intercalating into the multilayers in the place of lithium ions.

1.3. pH Sensors

1.3.1. Commercial pH Sensors

Currently, the most commonly used pH sensors include glass electrodes and single use pH strips.[69] Glass electrodes are potentiometric sensors which rely on a differential in ions in the reference solution and environment. This causes a potential difference which can be used to calculate pH based off the Nernst Equation (Eq. 7):[62,70,71]

$$E = E^o + \frac{2.303RT}{nF} \log (H_3O^+) \quad (7)$$

where E is the potential difference across the glass membrane, E^o is standard cell potential, R is the gas constant (8.314 J/mol/K), T is temperature (K), n is the valence of the electron (1 in the case of H_3O^+), F is Faraday's constant (96,485 C/mol), and (H_3O^+) is the concentration of H_3O^+ in the external solution.

At room temperature, the Nernst Equation can be reduced to the following equation (Eq. 8) where the ideal Nernstian response sensitivity of 59.16 mV/pH is given as the slope:[62]

$$E = E^o - 0.05916 \text{ pH} \quad (8)$$

where E is the potential difference across the glass membrane and E^o is standard cell potential.

Additionally, the temperature term seen in the Nernst Equation indicates the temperature dependence of pH readings and necessitates regular calibration. On the other hand, pH strips are made of a chemical indicator that changes color in response to changes in pH.[60] This occurs due to the protonation/deprotonation of the indicator in different pH regimes which explains why pH strips give ranges of pH for each color displayed. This makes pH strips simple to use and interpret.

However, both methods have their limitations. Glass electrodes, while accurate, have limited functionability in extreme pH regions and require consistent upkeep to maintain their performance. Due to the materials of construction of the electrode, it is also very fragile. The glass is prone to breaking and the electrode can dry out if exposed to air. Either of these occurrences would render the electrode unusable. Additionally, the glass electrode is a potentiometric sensor and is limited in sensitivity by the Nernstian limit. On the other hand, pH strips have the benefit of being easy to use but lack robustness and resolution. Due to the colorimetric response of the strips, it is not possible to determine an accurate pH, only a range.

1.3.2. Literature Review of Current pH Sensors

To date, most novel pH sensors have typically been potentiometric or a subset of field effect transistors (FETs), each of which having its own advantages and disadvantges.[62] However, both of these types of pH sensors use the same figure of merit

(mV/pH) as conventional glass electrodes which makes them all comparable to the maximal Nernstian response, leading to their prevalence. Despite this, there has been interest in a variety of other sensor types such as colorimetric and resistive due to their ease of use.[39,63] Table 1 includes some current pH sensors along with their materials of construction and notable figures of merit. As the focus of this thesis is on resistive sensors, the table includes more examples for this sensor type.

Table 1. Review of current pH sensors.

Material	**Type**	**pH Sensitivity**	**pH Range**
Solution gated epitaxial graphene[56]	GFET	98-99 mV/pH	2 – 12
PdO[72]	EGFET	62.87 mV/pH	2 – 12
WO_3[73]	Potentiometric	-56.7 mV/pH	5 – 9
PANI[74]	Potentiometric	63.3 mV/pH	3 – 8
$CeTi_xO_y$[59]	Potentiometric	89.81 mV/pH	2 – 12
$(PDDA/PSS)_3(PDDA/PEC^-)_{10}$[75]	Interferometer	0.6 nm/pH acidic region -0.85 nm/pH basic region	2 – 11
Ti_3C_2 QD[39]	Optical		5 – 9
$(PAH/NR\text{-}PAA)_{15}$[76]	Optical		3 – 9
MQD-GO[61]	Optical		1 – 7
SWNT-PANI/PVA[77]	Resistive	20 kΩ/cm^2/pH	1 – 10
p-SWNT-PSS/PANI[54]	Resistive	4.56 kΩ/cm^2/pH acidic region 20.66 kΩ/cm^2/pH basic region	0.95 – 12
Graphene[63]	Resistive	2 kΩ/pH	4 – 10
MWNT[78]	Resistive	65 Ω/pH	5 – 9
ES-PANI/PVB[79]	Resistive	0.28 MΩ/pH	1 – 8
Pd[80]	Resistive	5 %/pH	4 – 10
MWCNT/Ni[81]	Resistive	1 %/pH	2 – 10

1.4. Thin Film Assembly Methods

1.4.1. Spray

Spray coating films is a facile and scalable method for producing thin films. An aqueous dispersion of the desired coating material is used as feed for a spray gun. Using pressurized air, the dispersion is propelled from the spray gun as an aerosol mist onto the desired substrate. By heating the substrate throughout the process, it becomes possible to heat off the solvent of the dispersion and obtain a thin film of the desired material.[82] However, this leads to nonuniform films as both deposition and drying are often nonuniform due to how the spray gun is moved throughout the coating process and a nonuniform heat profile respectively. This method typically results in relatively thicker and rougher films that lack a hierarchical structure as compared to LbL assembly.

Recently, Weng *et al.* explored the use of spray assembly in spin spray layer-by-layer assembly.[83] Their novel thin film assembly method is highly tunable (spin rate, spray time, and concentration) and has allowed for deposition of layer pairs of thickness down to 0.55 – 0.7 nm.[83] Alternating layers of positively and negatively charged materials are spray onto a heated substrate that is kept spinning throughout coating which improves homogeneity of the coating. As opposed to typical spray coating, this allowed for the creation of a thin film with tunable composition and thickness with a hierarchical structure.

1.4.2. Drop Casting

Drop casting is a facile method for making thin films. The method involves "dropping", often done by pipetting, an aqueous solution of the desired coating material

onto the substrate. However, this method is not always feasible as it results in relatively thick film as compared to other thin film fabrication methods and often leads to nonuniform coatings due to uneven dispersion and drying of the solution.[66] Drop casting is a common coating method for sensors on glassy carbon electrodes (GCE) due to the facile assembly method.[84-87] After drop casting, the performance of the coated GCEs can then be evaluated using electrochemical testing methods such as cyclic voltammetry or amperometry.

1.4.3. Layer-by-Layer Electrostatic Self-assembly

Layer-by-layer (LbL) electrostatic self-assembly is a method for making thin films with layers of alternately charged materials.[88-90] By using materials of opposing charge in adjacent layers, electrostatic attraction between the layers occurs. This allows for self-assembly of multilayers to occur. Due to the electrostatic attraction, the produced films are extremely stable and result in a highly ordered structure.[88] The ability to form a thin film with layers of varying properties allows for control of the bulk film properties. This creates the possibility of choosing constituent materials and assembly conditions (e.g. deposition time, number of layer pairs, deposition concentration) to tune the film properties to specific applications. Additionally, this method is extremely versatile and allows for conformal coatings on a variety of substrates.[40,91] More recently, Cai *et al.* demonstrated that this assembly procedure allows for improved sensor performance as compared to direct mixing.[65]

1.5. Constituents for Layer-by-Layer Assembly

Given their promising properties for pH sensing, MXenes, in this case $Ti_3C_2T_x$, will be used as one of the main components in the resistive sensor. Due to their functionalized surface, MXenes have the potential to adsorb the positively charged ions surrounding them. As demonstrated by VahidMohammadi *et al.* for the case of V_2CT_x, positively charged ions, cations, will readily intercalate into the MXene multilayers and cause a shift in d-spacing. As d-spacing changes, so too does the conductive pathway and the resistance of the MXene multilayers. Additionally, the hydroxyl surface groups of the MXene can protonate/deprotonate which will affect the number of cations that can interact with the MXene. One concern of using NaAsc is the salt concentration due to the presence of sodium salt. While salt concentration can affect both colloidal stability and LbL assembly, the molarity of the sodium ascorbate in the $Ti_3C_2T_x$ dispersion is sufficiently low as to not cause issue. Given the molecular weight of NaAsc (197.11 g/mol), the concentration of NaAsc in the dispersion is 0.005 M. $Ti_3C_2T_x$ dispersions have been demonstrated to be stable up to 0.05 M salt concentrations.[50] More recently, the ion intercalation has shown promise as a way to improve the sensitivity of $Ti_3C_2T_x$ sensors.[67] As such, the findings of Koh *et al.* have supported an additional benefit of the inclusion of NaAsc.

Due to the negative charge of MXenes, a positively charged polymer, a polycation, is necessary for successful electrostatic self-assembly to occur. The two polycations explored herein are poly (diallyldimethylammonium chloride) (PDADMAC) and branched polyethylenimine (BPEI). PDADMAC was chosen due to its pH insensitivity.

This insensitivity is due to PDADMAC being a strong electrolyte and maintaining its positive charge throughout the entire pH range.[92] The structure of PDADMAC is shown in Figure 1.

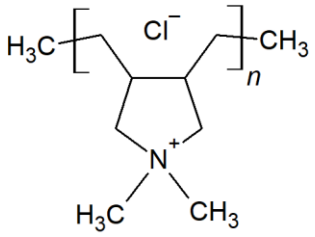

Figure 1. Structure of poly (diallyldimethylammonium chloride).

To demonstrate the effects of using a highly pH sensitive polymer, BPEI was used to contrast PDADMAC. Its high sensitivity can be attributed to its variety of amine groups: primary (pKa = 4.5), secondary (pHa = 6.7), and tertiary (pKa = 11.6).[93] The structure of BPEI is shown in Figure 2.

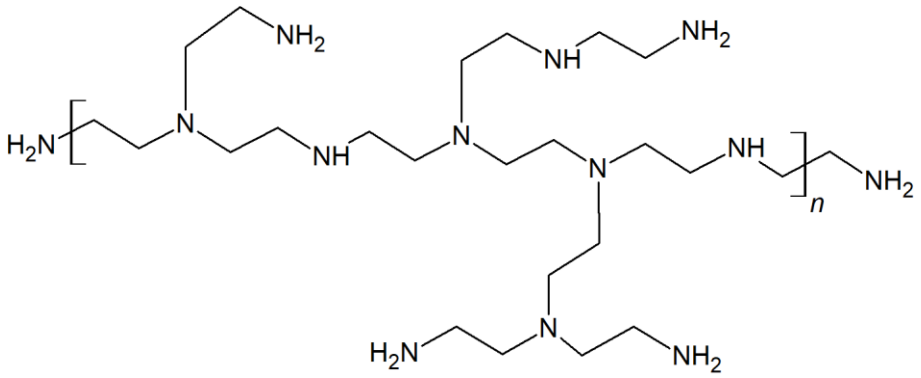

Figure 2. Structure of branched polyethylenimine.

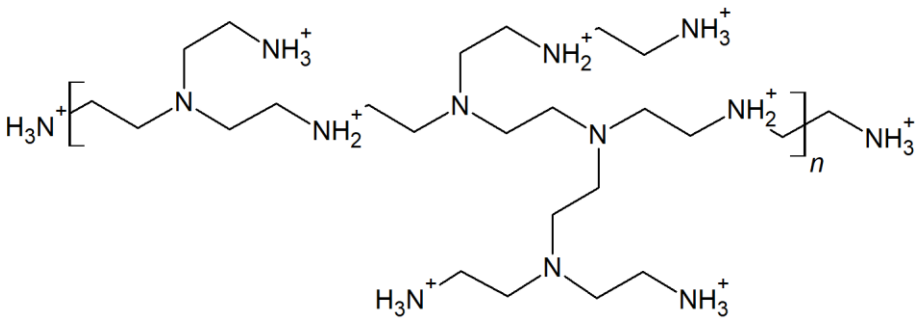

Figure 3. Structure of branched polyethylenimine with protonated secondary and tertiary amine groups.

As the pH of BPEI changes, the degree of protonation of the amine groups will vary as well which results in a conformational change in the polymer. When the pH is lower than the pKa, the respective amine group will become protonated and vice versa. For example, in Figure 3, the secondary and tertiary amine groups of BPEI are protonated. This is indicative of the pH being between pH 4.5 and pH 6.7 and results in a positively charged

polymer. As the charge density changes, a varying amount of electrostatic interaction is present, and the polymer chains can either aggregate or extend, causing a change in thickness. Due to this pH induced change in thickness, BPEI shows promise as a material in a resistive pH sensor.

As a control for the MXenes, reduced graphene oxide (rGO) will also be used in conjunction with both polymers to make multilayers. As mentioned before, rGO and MXenes are both two dimensional carbides with high conductivity. MXenes have shown potential in a bulk of applications that rGO and graphene oxide (GO) have already been applied to. However, in the case of LbL assembly, an aqueous solution of the material is required. As GO is hydrophilic and dispersible in water, film assembly will be done using GO and the prepared film will be reduced to obtain rGO based multilayers.

2. EXPERIMENTAL

2.1. Materials

Melinex ST505 (Polyethylene terephthalate (PET) substrates) was purchased from Tekra. Acetone (>99.5%), isopropyl alcohol (IPA, >98%), slide glass, and 5 MHz Ti/Au quartz crystal substrates were purchased from VWR. 18.2 MΩ·cm (Milli-Q) water was obtained using Milli-Q Integral Water Purification System for Ultrapure Water. Poly(diallyldimethyl ammonium chloride) (PDADMAC, MW = 200,000 to 350,000 g/mol, 20 wt% in water), branched polyethyleneimine (BPEI, MW = 25,000 g/mol, MN = 10,000 g/mol), hydrochloric acid (HCl, ACS reagent, 37% w/w), sodium hydroxide (NaOH), potassium permanganate (KMnO4), sodium nitrate ($NaNO_3$), sodium hydroxide (NaOH), potassium permanganate (KMnO4), dimethyl sulfoxide (DMSO, ReagentPlus, >99.5%), and sodium L-ascorbate (NaAsc, crystalline, >98%) were purchased from Sigma-Aldrich. Titanium (Ti, 44 μm average particle size, 99.5% purity), aluminum (Al, 44 μm average particle size, 99.5% purity), titanium carbide powders (TiC, 2 – 3 μm average particle size, 99.5% purity), lithium fluoride (LiF, 98+% purity), hydroiodic acid (HI, 55%), and silver conductive adhesive paste (sheet resistance <0.025 Ω/□ at 0.001" thick) were purchased from Alfa Aesar. Type E polytetrafluoroethylene (PTFE) 18 American wire gauge (awg) 19 Strands (silver plated copper wire) was purchased from WesBell Electronics, Inc. Sulfuric acid (H_2SO_4, 95 – 98%), potassium hydroxide (KOH), and hydrogen peroxide (H_2O_2, 30%) were purchased from BDH. Graphite (SP-1) was purchased from Bay Carbon. Si wafers were purchased from University Wafers.

2.2. Ti_3AlC_2 MAX Powder Synthesis

Ti_3AlC_2 MAX powder was synthesized using commercial Ti, Al, and TiC powders as received following previous reports.[64] The powders were weighed and combined in a Ti:Al:C = 3:1.2:1.8 ratio and subsequently mixed by ball milling with zirconia beads at 300 rpm for 24 hours in a glass jar. The bulk Ti_3AlC_2 sample was then sintered at 1510 ºC with a loading of 50 MPa for 15 minutes using Pulsed Electric Current System (PECS). The sample was then drill milled and sieved to obtain high purity powder with 20 to 45-micron particle size.

2.3. $Ti_3C_2T_x$ Clay Synthesis

Following previous reports, $Ti_3C_2T_x$ clay was synthesized from the MAX phase by selective etching of the aluminum.[3,64] Hydrochloric acid (HCl, 37% w/w) was diluted to 6 M HCl in deionized (DI) water. The solution was placed in a polypropylene beaker and LiF was subsequently added. The dispersion was continuously stirred for 5 minutes at room temperature using a Teflon magnetic stirrer. The MAX phase powder was slowly added to the solution due to the exothermic nature of the reaction. The beaker was capped to prevent evaporation and a hole was made to mitigate gas build up. The mixture was then stirred at 40 ºC for 45 hours. The product was filtered using DI water in a polyvinyl difluoride (PVDF) filtration unit with 0.22-micron pore size (Millipore® SCQVU10RE StericupTM GV) and washed until the pH of the solution reached 6 to ensure any

remaining hydrofluoric acid (HF) was removed. The material remaining on the filter was collected as the $Ti_3C_2T_x$ clay.

2.4. $Ti_3C_2T_x$ Clay Intercalation and Delamination

An aqueous dispersion of $Ti_3C_2T_x$ was obtained by intercalation of the clay with dimethyl sulfoxide (DMSO) and delamination by bath sonication as done in previous reports.[64] A 60 mg/mL suspension was created by adding 1mL of DMSO to 60 mg of the clay. The suspension was stirred at room temperature for 20 hours to fully intercalate the clay. Remaining DMSO was removed by solvent exchange by washing suspension with DI water and centrifuging for 4 hours at 5000 rpm. The resulting suspension was bath sonicated for an hour at room temperature and subsequently centrifuged for an hour at 3500 rpm. The resulting supernatant contained the $Ti_3C_2T_x$ dispersion. Concentration of the dispersion was determined by vacuum filtration of a known volume of dispersion and subsequent weighing of the film. The $Ti_3C_2T_x$ dispersion was diluted in Milli-Q water to obtain a 0.5 mg/mL dispersion, and 1 mg/mL of NaAsc was added to mitigate oxidation.

2.5. Graphene Oxide Synthesis

Graphene oxide (GO) was synthesized following the Modified Hummers' Method.[94] 3 g of graphite powder and 2.5 g of $NaNO_3$ were added to 120 mL of concentrated H_2SO_4. The mixture was then stirred in an ice bath for 5 hours. After this time, 15 g of $KMnO_4$ was slowly added while the mixture stirred continuously. The temperature of the mixture was kept below 20 ^oC throughout mixing. The mixture was

then diluted with 700 mL of cold ultrapure water and 20 mL of hydrogen peroxide. Addition of hydrogen peroxide caused the color to change to brown. The mixture was then washed with 5 wt% HCl and filtered. The filtered mixture was dispersed in ultrapure water and subsequently dialyzed against ultrapure water. Dialysis was repeated until mixture pH reached the pH of ultrapure water. The remaining powder was then dried at 60 ^{o}C and redispersed in water to obtain a 0.5 mg/mL solution of GO. The dispersion was then sonicated to obtain a stable dispersion.

2.6. Layer-by-Layer Film Assembly

LbL polymer and $Ti_3C_2T_x$ composites were prepared on glass, silicon (Si) wafers, polyethylene terephthalate (PET), and quartz crystal substrates following procedure from An *et al.*[40,64] The polymers used were PDADMAC and BPEI, the former was used at its natural pH (pH 7.8) and the latter at pH 5 to control the assembly conditions of the film. pH was adjusted using HCl. At pH 5, the primary and secondary amine groups of the BPEI are protonated and the polymer is positively charged. PDADMAC was used due to its pH insensitivity whereas BPEI allowed for an opposing view due to its high pH sensitivity. Both polymers were diluted to 1 mg/mL in Milli-Q water whereas $Ti_3C_2T_x$ and GO were diluted to 0.5 mg/mL in Milli-Q water. Glass slides (6 cm x 2.5 cm x 1 mm) were cut to dimensions of 5 cm x 1.25 cm x 1 mm using a diamond glass cutter. Glass substrates were bath sonicated in IPA for 15 minutes. The substrates were then cleaned with water and acetone in that order and air dried after both cleanings. The PET substrates were cleaned with water and isopropyl alcohol. After cleaning, the substrates were plasma treated

(Harrick PDC-32G) for 3 minutes to create a hydrophilic surface for the positively charged polymer to adsorb to. 4 lines of tape (1 mm x 4 mm) were placed lengthwise on the PET substrates to create U-shaped patterns. The plasma treated substrates were then submerged in the polymer for 15 minutes. The substrates were then submerged in Milli-Q water three times for 1 minute each time and subsequently air dried. The same coating procedure was used for $Ti_3C_2T_x$. Coating with both materials constituted one bilayer pair and these steps were repeated to achieve the desired layer pair (LP) number. For the quartz crystal substrates, the cleaning procedure was the same as for PET substrates. Coating procedure was identical to the previously mentioned procedure but was done while the quartz crystal was attached to the Quartz Crystal Microbalance (QCM, MAXTEK RQCM Research Quartz Crystal Microbalance Monitor). After coating, the PET films were cut in half to halve the resistance of the film and increase the number of sensors produced. Due to the conductive pathway being along the length of the film, variations sensor length, and subsequently path length, can be used to modify bulk film resistance. The halved films were subsequently cut into four strips (0.31 cm x 2.5 cm) with each having a U-shaped pattern. Silver coated copper wires were then placed on each side of the top of the 'U' and attached to the film using silver paste. The silver paste was then dried by placing the film in a vacuum oven at room temperature for 6 hours. The final path length of the sensors from lead to lead was ~4.1 cm with a width of ~0.11 cm. Due to the bottom of the 'U' being thicker than 0.11 cm, the total surface area was 0.58 cm^2.

2.7. Preparation of Reduced Graphene Oxide Based Films

Due to the ease of processability and hydrophilicity of GO, rGO based thin films were fabricated by the chemical reduction of GO based films.[82] Reduction of GO based films was necessary due to the low conductivity of GO. LbL assembly of graphene oxide films followed the previous procedure using GO in place of $Ti_3C_2T_x$. However, an additional reduction step was performed prior to cutting the films to create the sensors. GO reduction was carried out using hydroiodic (HI) vapor.[82] 1 mL of 55% HI was added to a glass petri dish containing the GO based film. This petri dish was stored in a secondary glass petri dish to prevent HI vapor from escaping, and the outer petri dish was subsequently covered and sealed with paraffin. The petri dish was then heated at 90 ^oC for 8 minutes to achieve adequate reduction following the findings from De *et al*.[82] The reduced film was then washed with ethanol. Reduction was verified by color change and resistance decrease of the film. The (polymer/rGO) multilayers on PET were then made into sensors as described previously. Characterization of rGO based films was done prior to reduction. Based on previous reports, rGO films will become approximately 5% thinner after reduction.[82]

2.8. Preparation of Spray-Assembled $Ti_3C_2T_x$ Films

$Ti_3C_2T_x$ films were prepared by spray coating using a procedure combining those of Zhao *et al.* and De *et al*.[82,95] Patterned PET substrates were placed on a heating plate set to 90 ^oC. A 0.5 mg/mL $Ti_3C_2T_x$ dispersion was sprayed onto the substrate from a vertical distance of 15 cm for 8 minutes with constant movement (1 cm/s) of the nozzle to

prevent aggregation. Nozzle pressure was maintained at 80 psi. The coated substrate was cut and prepared into sensors as previously described.

2.9. Film Growth and Characterization

2.9.1. Profilometry

Film thickness and roughness were determined by profilometry (KLA Tencor D-100). Measurements were taken every layer pair to create a growth profile of the film. The profilometer can determine thickness and roughness of the film by performing a topographical scan of the surface. A thin stylus is lowered onto a surface and physically moves along the film. The height change of the stylus is directly correlated to the thickness of the film. By measuring a pristine and coated portion of the substrate, the film thickness (t) is the delta height of the two regions. Root mean square (RMS) roughness (R_q) can be calculated from the height profile of the film. All measurements were repeated a minimum of three times. A pristine portion of the substrate was obtained by making a vertical scratch along the film. It was ensured that only the film was removed and that the glass was not scratched to prevent inaccurate measurements. All layer growth characterization of rGO based multilayers was done prior to reduction.

2.9.2. Ellipsometry

Film thickness was verified using an ellipsometer (LSE Stokes Ellipsometer)**.** A pristine substrate was first measured to determine the refractive index (N) and extinction coefficient (K) of the substrate. t and N of the films were then determined using a thin

oxide model. *t* guesses were taken from profilometry results. For this method, a reflective surface is required, so coated Si wafers were used for these measurements. A minimum of three measurements were taken for every sample, including the pristine substrate used for the baseline.

2.9.3. Spectrophotometry

As more $Ti_3C_2T_x$ or GO is deposited onto the film and the thickness increases, so too will the absorbance of the thin as the film will become darker. Subsequently, spectrophotometry can be employed to quantify this increase in absorbance. The absorbance of note occurs at 770 nm and 335 nm for $Ti_3C_2T_x$ and GO respectively. Absorbance was measured using a solid-state spectrophotometer (Shimadzu SolidSpec-3700 UV-VIS-NIR Spectrophotometer) using a pristine glass slide for baseline measurements. A light of known intensity is passed through the solid substrate at varying wavelengths (scanning from 800 nm to 300 nm). The intensity of the light after travelling through the film is then measured to determine how much light was absorbed at each wavelength following Eq 9.

$$A = \log (I/I_o) \quad (9)$$

where A is absorbance at a specific wavelength, I is beam intensity after passing through the sample, and I_o is initial beam intensity. The ratio of intensities is equivalent to transmittance.

2.9.4. Film Composition

Using a Quartz Crystal Microbalance (QCM), film composition can be determined for a thin film coated on substrates of certain materials, in this case quartz. The QCM measures the change in frequency of the film after each deposition step. Using the Sauerbrey equation (Eq. 10), the change in frequency can be converted into mass change.

$$\Delta f = \frac{-2f_o^2}{A\sqrt{\rho_q \mu_q}}\Delta m \quad (10)$$

where Δf is the change in frequency, f_o is the resonant frequency (Hz), Δm is the change in mass, A is the area between electrodes (cm^2), ρ_q is the density of quartz (2.68 g/cm^3), and μ_q is the shear modulus of quartz crystal (2.95 x 10^{11} $g/cm/s^2$).[96,97] By measuring mass deposited every half layer pair, the mass contribution from each component can be determined and an overall composition by mass fraction can be obtained.

2.9.5. MAX and MXene Characterization

Chemical composition of both MAX phase, $Ti_3C_2T_x$ nanosheets, and $Ti_3C_2T_x$ multilayers was obtained. Deconvoluted x-ray photoelectron spectroscopy (XPS, Omicron XPS/UPS system with Argus detector) was used to determine the bond types of the relevant elements (e.g. Ti, C, O, and F). This verifies the removal of Ti-Al bonds and the creation of Ti-O and Ti-F bonds due to surface functionalization. Additionally, XPS can be used to check for over etching by the presence of C-C bonds which would be caused by the generation of carbide derived carbons (CDC) which are a byproduct of over etching. Samples for XPS were prepared by freeze drying a dispersion of $Ti_3C_2T_x$. XPS samples for sensors before and after testing were prepared by drying the sensor at room temperature

under vacuum for a minimum of three days. X-ray diffraction (XRD, Bruker D8 powder X-ray diffractometer fitted with LynxEye detector) of the MAX phase and $Ti_3C_2T_x$ nanosheets verified successful etching of the 'A' phase from the MAX phase powders. This can be seen quantitively as the downshift of the (002) peak from the MAX phase to the MXene and the disappearance of peaks around 30^o to 40^o. Secondary electron microscopy (SEM, JEOL JSM-7500F) of the nanosheets verifies that delamination was successful. XRD, XPS, and SEM samples for the initial $Ti_3C_2T_x$ dispersion were prepared by freeze drying a dispersion of $Ti_3C_2T_x$. Samples for SEM and XPS of sensors were used as prepared. Atomic force microscopy (AFM, Bruker Dimension Icon AFM) was used to measure nanosheet thickness and lateral size. Samples for AFM were prepared by drop casting on mica. Zeta potential and particle size of a dispersion of 0.5 mg/mL $Ti_3C_2T_x$ were measured using a Malvern Zetasizer Nano ZS. Dynamic light scattering (DLS) was employed to measure the latter.

For XPS peak fitting, Ti 2p, C 1s, O 1s, and F 1s spectra were deconvoluted based off of previous reports using CasaXPS software.[49,98] Due to the low AT% of N 1s and Cl 2p, these components were not deconvoluted. To determine background contribution, a Shirley type background function was applied to all spectra. The spectra were then calibrated based on the adventitious carbon peak (C-C,284.8 eV) prior to peak fitting. To ensure accurate peak fitting results, all binding energies (eV) were verified with previous literature results and full width half maximum (FWHM) values were constrained.[49,98] For the Ti 2p spectra, contributions were split into the $2p_{3/2}$ and $2p_{1/2}$ spin components. The area ratio of the two was set to 2:1 $2p_{3/2}$:$2p_{1/2}$. The components used for each

deconvolution are as follows: Ti-C, Ti^{2+}, Ti^{3+}, TiO_2, and TiF_x for Ti 2p, C-Ti-T_x^a, C-Ti-T_x^b, C-C, CH_x/CO, C-OH, and COO for C 1s, TiO_2, C-Ti-O_x, C-Ti-$(OH)_x$, Al_2O_3, and H_2O for O 1s, and C-Ti-F_x and AlF_x for F 1s. As the C-Ti-T_x bond is asymmetric, it was represented by two symmetric peaks.[49,98] All binding energies, FWHM, and AT% values were then quantified and tabulated.

2.10. pH Response Testing

All response testing was done at room temperature (25 ^oC). Prior to response testing, the sensor was submerged in Milli-Q water for 24 hours to allow the multilayers to fully swell. Due to the hydrophilic nature of $Ti_3C_2T_x$, water can readily intercalate into and adsorb to $Ti_3C_2T_x$ sheets which increases resistance of the sensor. Additionally, polyelectrolyte layers undergo swelling with water as well.[99,100] As such, it is necessary to allot adequate time for the sensor to swell to mitigate swelling effects on sensor resistance.

After swelling, the sensor was submerged in 150 mL of Milli-Q water. pH and resistance were recorded in-situ using a commercial pH probe (Beckman Model 350 pH/Temp/mV Meter) and a multimeter (Dawson DDM645) respectively. The multimeter applied a direct current (DC) voltage of 1000 V. pH was adjusted using 0.05 M stock solutions of hydrochloric acid (HCl) and sodium hydroxide (NaOH). pH and resistance were recorded at various intervals from pH 3 to pH 7 with cycling to check for hysteresis and repeatability.

3. RESULTS AND DISCUSSION

3.1. MAX Phase and MXene

3.1.1. Chemical Characterization

XRD data was obtained for both the MAX phase and $Ti_3C_2T_x$ nanosheets as shown in Figure 4.

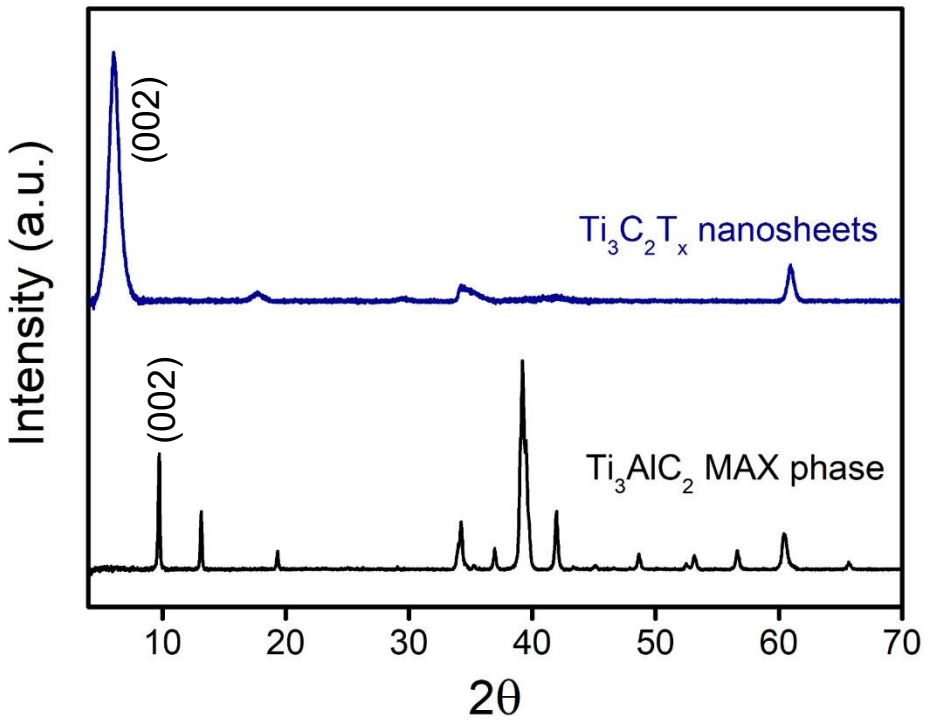

Figure 4. XRD of $Ti_3C_2T_x$ nanosheets and MAX phase.

Figure 4 depicts the peaks associated with the (002) MAX phase material ($2\theta \sim 10$) and (002) $Ti_3C_2T_x$ ($2\theta \sim 7$).[49,64] XRD peaks can be used to determine d-spacing by Bragg's Law (Eq. 11).

$$n\lambda = 2d \sin\theta \quad (11)$$

where n is a positive integer, λ is wavelength, d is d-spacing, and θ is scattering angle. In accordance with Bragg's law, d-spacing is inversely proportional to 2θ, and the downshift in (002) peak from MAX phase to $Ti_3C_2T_x$ is caused by the increased interlayer spacing when Al is successfully etched. The removal of peaks at higher 2θ occurs due to the crashing out of larger particles during the final centrifugation of the delamination process.

XPS was performed using the $Ti_3C_2T_x$ nanosheets to confirm the presence and determine the bond types of Ti, O, C, and F as shown in Figures 5 and 6.

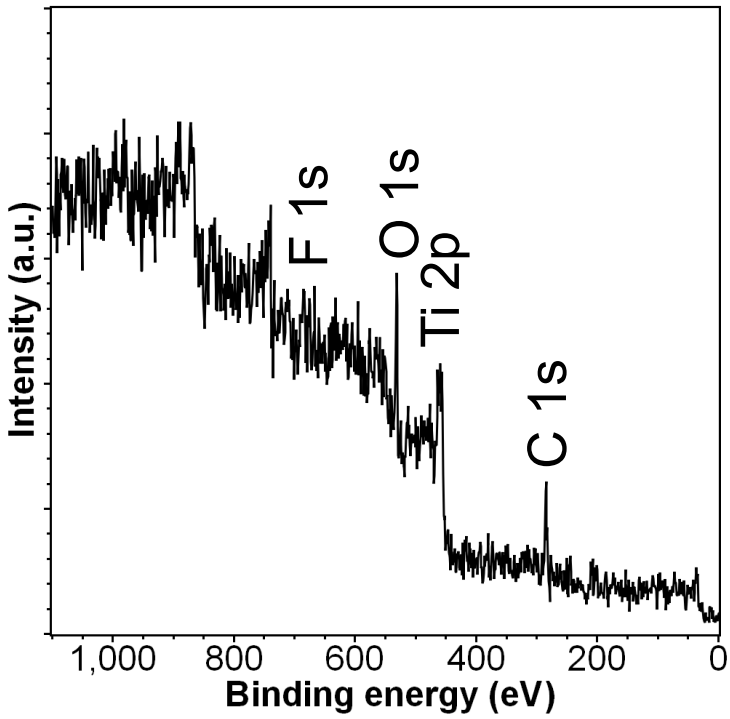

Figure 5. XPS survey scan of freeze dried $Ti_3C_2T_x$.

From the survey scan of $Ti_3C_2T_x$, the presence of Ti 2p, C 1s, O 1s, and F 1s is confirmed. These are the typical elements found in this MXene, and the absence of Al is indicative of the successful etching of Al from the Ti_3AlC_2 MAX phase. The peak fittings for each component are shown in Figure 6 with full width half maximum (FWHM) values, component atomic (at) %, and quantitative peak locations following in Table 2.[49,98] Numbers in parentheses correspond to the contribution from the Ti $2p_{1/2}$ orbital.

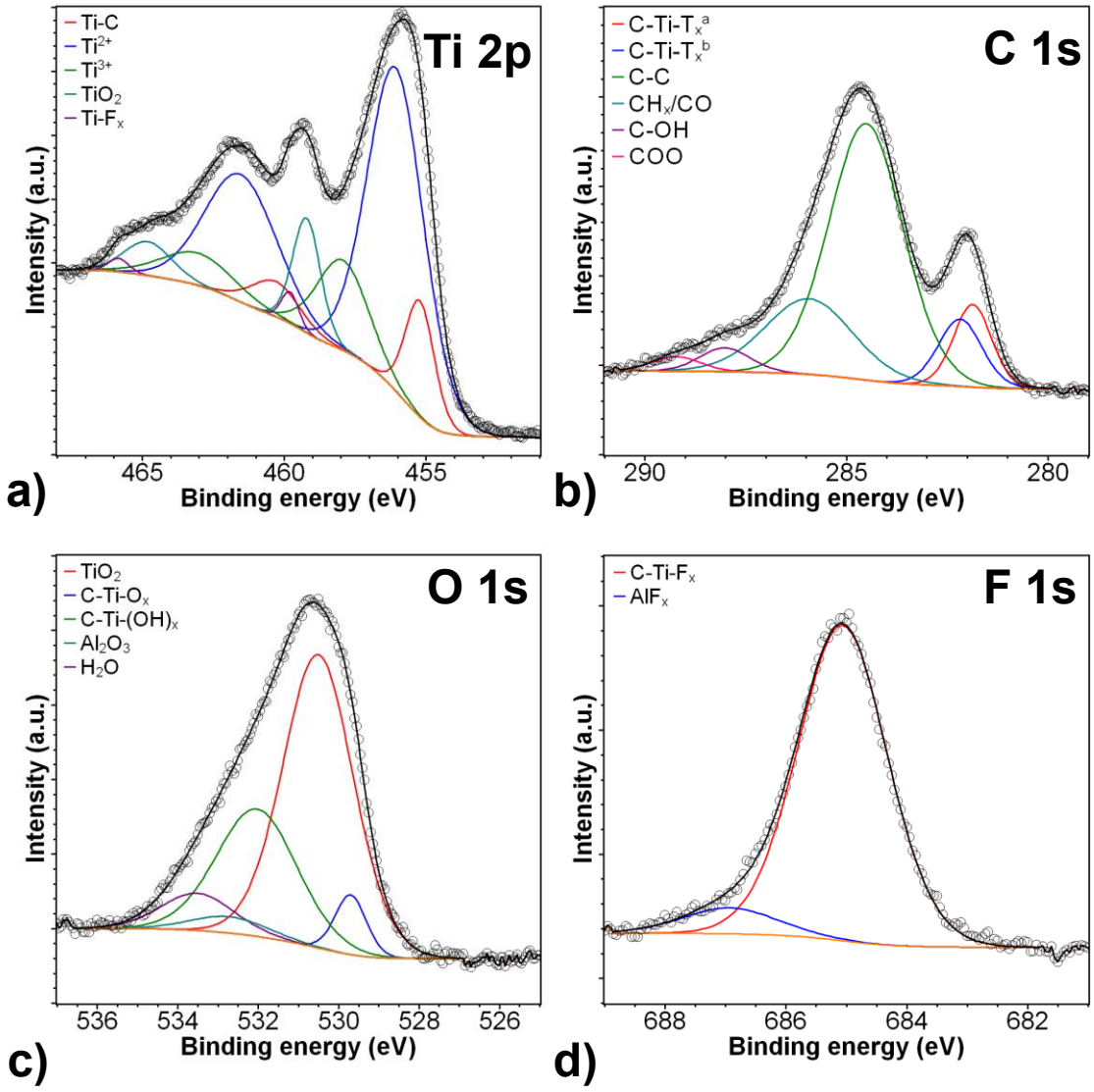

Figure 6. Component peak fittings of $Ti_3C_2T_x$ nanosheets for (a) Ti 2p, (b) C 1s, (c) O 1s, and (d) F 1s from XPS.

Table 2. XPS peak fitting results for $Ti_3C_2T_x$.

Element	Element at%	Binding energy (eV)	Component name	Component at%	FWHM
Ti 2p3/2 (2p1/2)	17.7	455.2 (460.3)	Ti-C	11.3	1.2 (2.0)
		456.1 (461.5)	Ti^{2+}	60.8	2.3 (3.0)
		457.9 (463.0)	Ti^{3+}	15.5	2.2 (3.0)
		459.2 (464.8)	TiO_2	10.6	1.2 (2.0)
		459.8 (465.8)	Ti-F_x	1.8	0.7 (0.8)
C 1s	54.2	281.9	C-Ti-T_x	9.3	1.1
		282.2	C-Ti-T_x	8.7	1.3
		284.5	C-C	56.7	2.2
		285.9	CH_x/CO	19.7	2.6
		288.0	C-OH	3.6	1.5
		289.2	COO	2.1	1.4
O 1s	22.9	529.7	TiO_2	5.1	0.9
		530.5	C-Ti-O_x	56.4	2.1
		532.0	C-Ti-$(OH)_x$	27.8	2.4
		532.7	Al_2O_3	3.4	2.2
		533.5	H_2O	7.3	2.1
F 1s	5.2	685.1	C-Ti-F_x	92.1	1.7
		686.9	AlF_x	7.9	1.8

For the Ti 2p peak fitting, the peaks of note occur for TiO_2 (459.2 and 464.8 eV) and Ti-C (455.2 and 460.3 eV).[49] The Ti-C peak demonstrates that M-X bonds have formed, and TiO_2 peaks would only be present when there are existing Ti-C bonds that can oxidize. The TiO_2 peaks also indicate the extent of oxidation of the MXene. The oxidation likely occurred during the freeze-drying process as the process can take days and the degree of oxidation is minimal. From the C 1s spectra, the presence of surface terminating groups is represented by two symmetric peaks at 281.9 and 282.2 eV. The two peaks represent an asymmetric peak corresponding to the surface terminal groups.[49] The

presence of -OH, -O, and -F surface functional groups is then confirmed by the O 1s and F 1s component fittings.

Zeta potential of a $Ti_3C_2T_x$ dispersion was measured as shown in Figure 7.

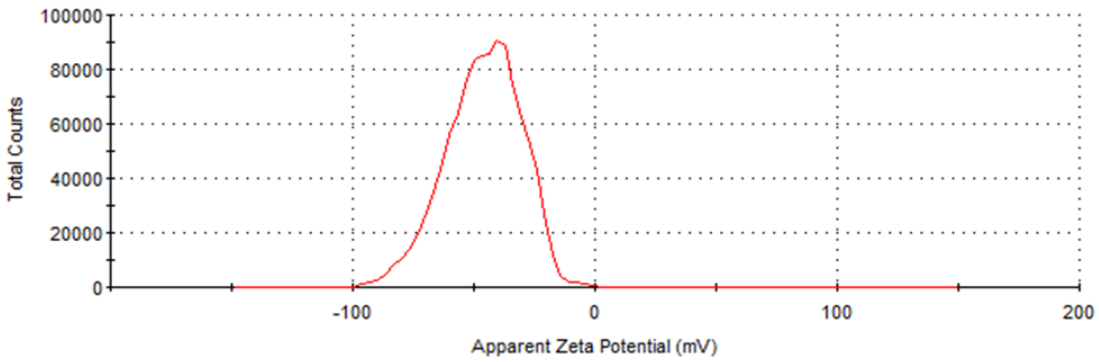

Figure 7. Zeta Potential Distribution of $Ti_3C_2T_x$.

The average zeta potential is -46.1 ± 15.1 mV. As zeta potential is correlated to surface charge, this verifies that the MXene is negatively charged and thereby a favorable component for LbL assembly with a positively charged counterpart. Additionally, the high absolute value of the zeta potential indicates that the dispersion is stable.[101]

3.1.2. Morphology

After delaminating the $Ti_3C_2T_x$ clay into nanosheets by sonication, a portion of the supernatant was freeze dried. SEM images of the powder were taken as shown in Figure 8.

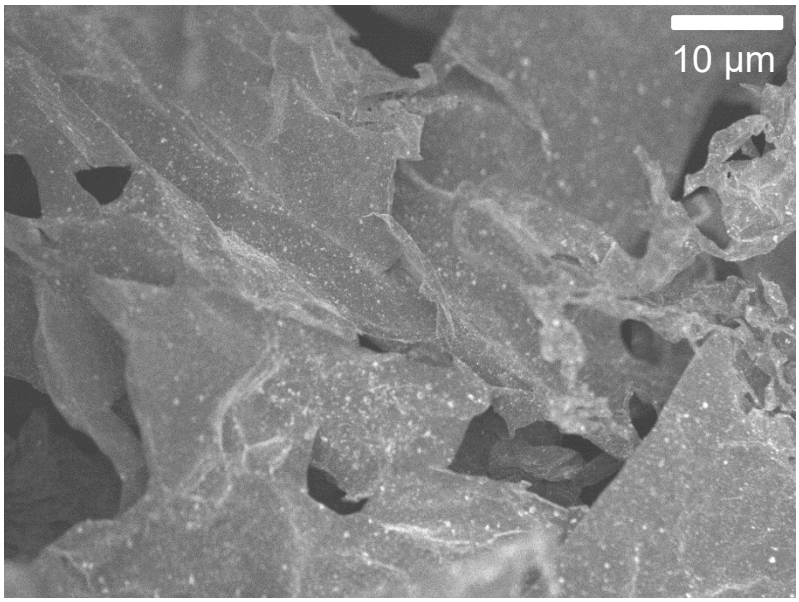

Figure 8. SEM of $Ti_3C_2T_x$ nanosheets.

As can be seen in Figure 8, the $Ti_3C_2T_x$ clay was successfully delaminated into nanosheets as opposed to the 'accordion' structure of the clay obtained just after etching. The white dots on the surface of the nanosheets are TiO_2 and indicative of oxidation of $Ti_3C_2T_x$. As the synthesis process from etching to nanosheets takes a minimum of 72 hours, and freeze drying takes an additional 72 hours, it is likely oxidation occurred during this time.

A topographical scan of $Ti_3C_2T_x$ nanosheets was obtained using atomic force microscopy (AFM) as shown in Figure 9a.

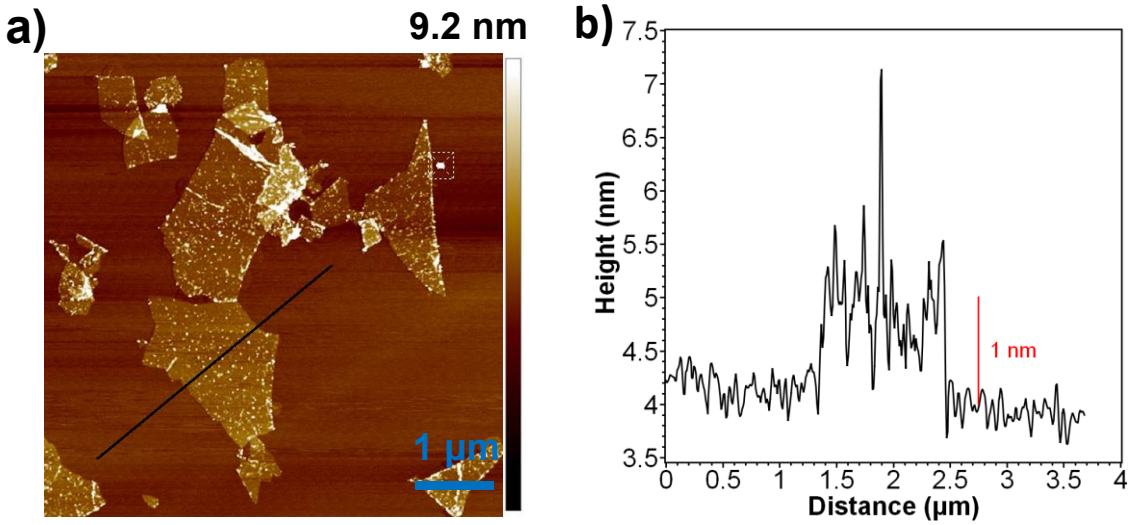

Figure 9. (a) Topographical scan and (b) height profile of $Ti_3C_2T_x$ nanosheets as measured by AFM.

The average thickness of the flakes was determined to be 1 nm (Figure 9b) which is in agreement with the theoretical thickness of nanosheets.[3] This indicates the presence of monolayer $Ti_3C_2T_x$. Lateral size of the nanosheets ranges from 0.6 to 2.3 micron. Smaller flake size can be achieved by longer and/or more intense sonication (e.g. tip sonication), but either of these would result in the sheets being more prone to oxidation as the surface area:volume ratio would increase.[48] Using DLS, the average hydrodynamic size of nanosheets in a dispersion of $Ti_3C_2T_x$ was measured to be 304.7 nm (Figure 10) which is in agreement with previous reports from literature.[36,67]

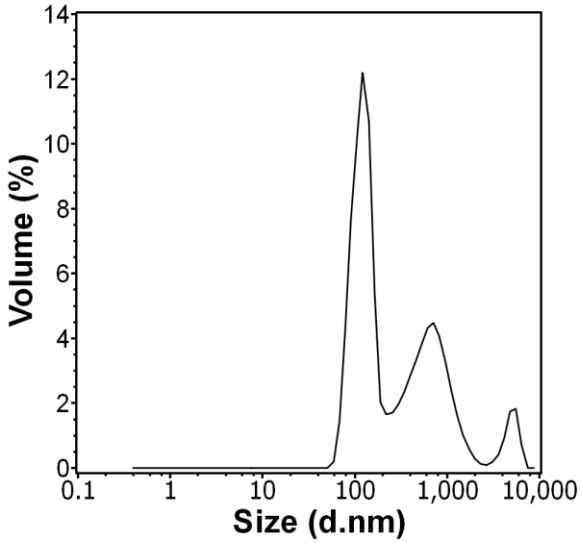

Figure 10. Size distribution of $Ti_3C_2T_x$ as measured by dynamic light scattering.

3.2. Layer Growth of Thin Films

As mentioned previously, films were prepared using the LbL assembly method. Assembly conditions for the polycations were 1 mg/mL at a pH of 7.8 for PDADMAC and pH 5 for BPEI. Nanomaterial dispersions were used at a concentration of 0.5 mg/mL. Layer growth of the $Ti_3C_2T_x$ films was first quantified by thickness and roughness using profilometry as shown in Figure 11.

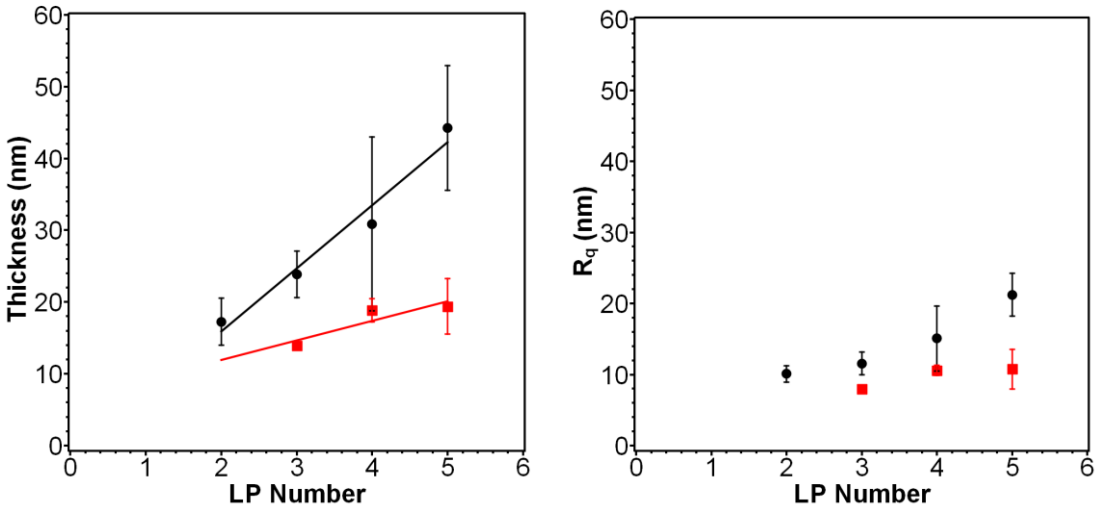

Figure 11. (a) Thickness and (b) RMS roughness of $Ti_3C_2T_x$ multilayers as measured by profilometry. Thickness increases as 8.8 nm/LP and 2.7 nm/LP for $(PDADMA/Ti_3C_2T_x)_y$ and $(BPEI/Ti_3C_2T_x)_y$, respectively.

As can be seen in Figure 11a, linear growth of the films is verified. The films grow at a rate of 8.8 nm and 2.7 nm per LP for $(PDADMA/Ti_3C_2T_x)_y$ and $(BPEI/Ti_3C_2T_x)_y$ respectively. The large error bars can be attributed to the relatively high roughness of the films. However, this roughness is below 25 nm for all films which demonstrates the fabrication of homogenous films. Based on the measured nanosheet thickness of 1 nm and the assumption that increases in thickness are dominated by the $Ti_3C_2T_x$ flakes, approximately 9 and 3 flakes are deposited each LP for $(PDADMA/Ti_3C_2T_x)_y$ and $(BPEI/Ti_3C_2T_x)_y$ respectively.[3,40]

Ellipsometry measurements were taken to reinforce the linear growth profile as shown in Figure 12.

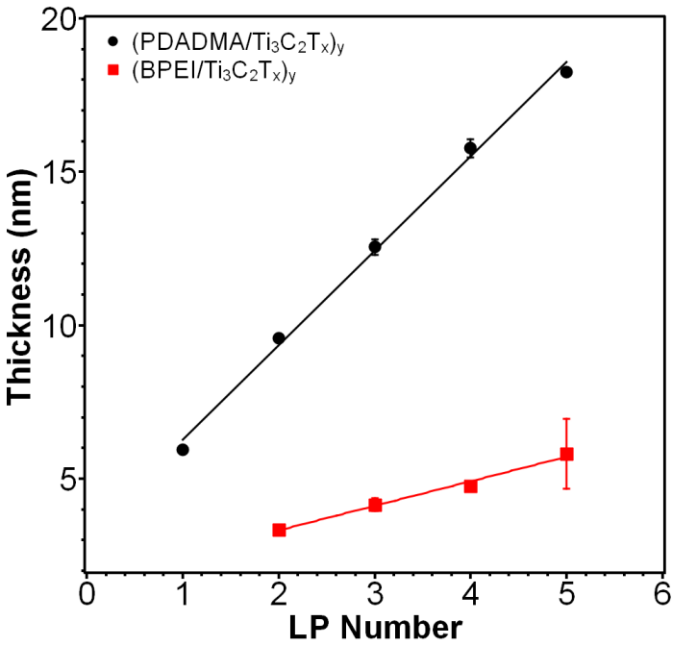

Figure 12. Thickness of $Ti_3C_2T_x$ multilayers as determined by ellipsometry. Thickness increases as 3.1 nm/LP and 0.8 nm/LP for $(PDADMA/Ti_3C_2T_x)_y$ and $(BPEI/Ti_3C_2T_x)_y$, respectively.

From ellipsometry, linear growth of the multilayers and higher thickness of $(PDADMA/Ti_3C_2T_x)_y$ films as compared to $(BPEI/Ti_3C_2T_x)_y$ films is confirmed. In the case, the thickness of $(PDADMA/Ti_3C_2T_x)_y$ films increases as 3.1 nm per LP. and the thickness of $(BPEI/Ti_3C_2T_x)_y$ films increases as 0.8 nm per LP. The difference in thickness from ellipsometry and profilometry can be attributed to two major factors. Firstly, ellipsometry relies on a variety of parameters including refractive index and extinction coefficient of the substrate and an estimate of the thickness of the film to solve for thickness. Since the parameters for the substrate are taken using a different, pristine substrate, there could be discrepancies between the coated and pristine substrates due to

the formation of silica on the surface of the wafer. While wafers are cleaned prior to coatings and measurements, it is still possible for this to cause issues. If the thickness guess for the film is inaccurate, it would also lead to incorrect results. Additionally, while LbL assembly is a versatile method, some substrates can still display different adhesion affinities. Due to this, the amount of polycation adsorbed in the first deposition could be lower which leads to reduced layer growth throughout. Despite the differences in thickness, the trend is still linear and the films with PDADMA grow at a considerably faster rate than those with BPEI. Ultimately, the thicknesses obtained from profilometry were taken to be more accurate as it is a more direct measurement of thickness.

Absorbance of films on glass substrates was measured using spectrophotometry as shown in Figure 13.

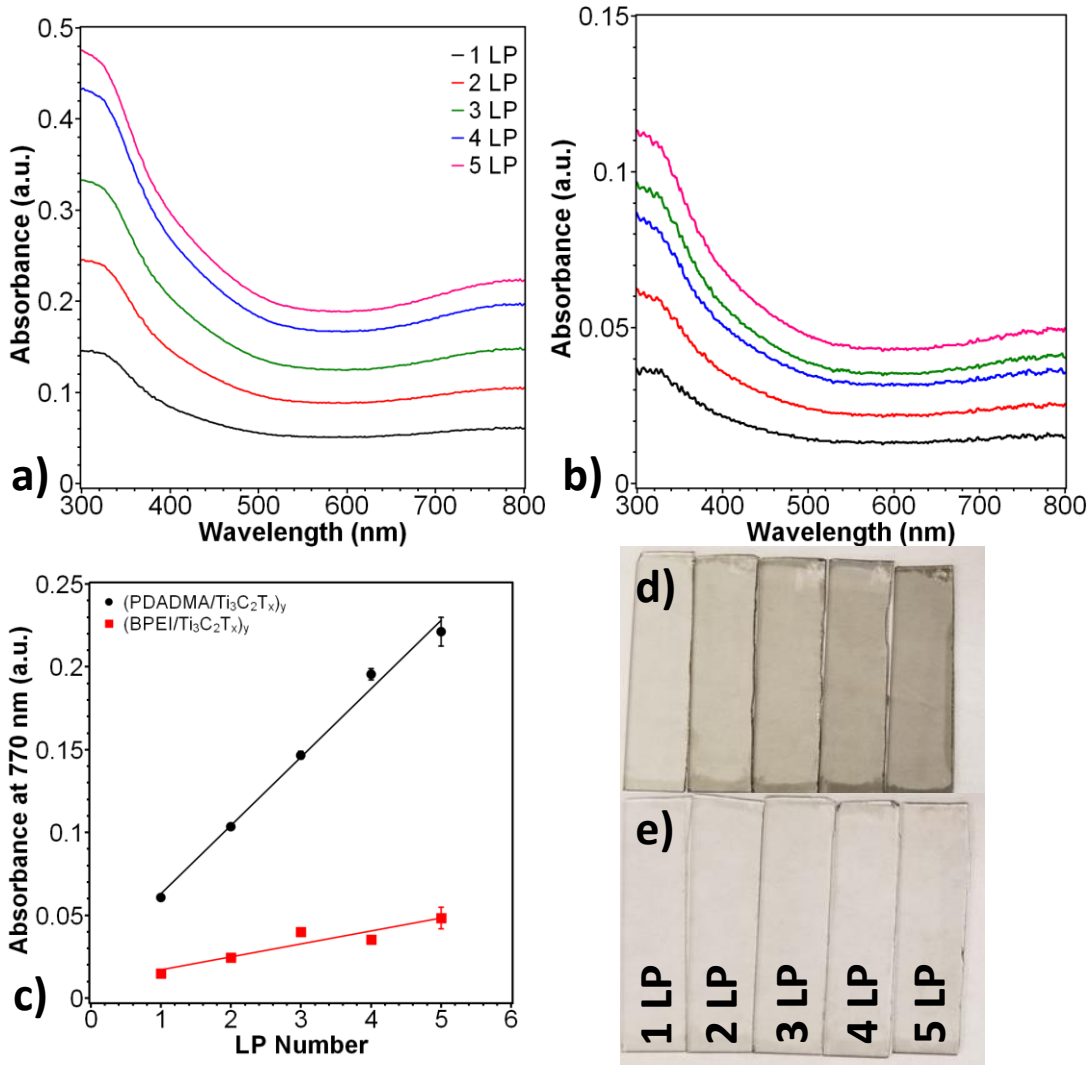

Figure 13. Absorbance of (a) $(PDADMA/Ti_3C_2T_x)_y$, (b) $(BPEI/Ti_3C_2T_x)_y$, and (c) $Ti_3C_2T_x$ multilayers at 770 nm as measured by spectrophotometry and digital images of (d) $(PDADMA/Ti_3C_2T_x)_y$ and (e) $(BPEI/Ti_3C_2T_x)_y$.

As can be seen in Figure 13c, linear growth of the films is once again verified, and the absorbance increases at a rate of 0.04 a.u. and 0.01 a.u. per LP for $Ti_3C_2T_x$ based films

with PDADMA and BPEI respectively. The absorbance can be correlated with the thickness as shown in Eq 12. for $(PDADMA/Ti_3C_2T_x)_y$ and Eq 13. for $(BPEI/Ti_3C_2T_x)_y$.

$$t\ (\text{nm}) = 77.0 * \text{absorbance (a.u.)} + 1.6 \quad (12)$$

$$t\ (\text{nm}) = 100.0 * \text{absorbance (a.u.)} + 0.8 \quad (13)$$

This relationship makes it possible to determine thickness of films coated on substrates that cannot easily be used for profilometry. One such example is PET due to the need to scratch off part of the surface. While this is not an exact measurement due to differences in substrate affinity, it can provide an order of magnitude guess and an accurate trend of layer growth.

Using QCM, the composition (wt%) for both constituent layers was determined (Figure 14).

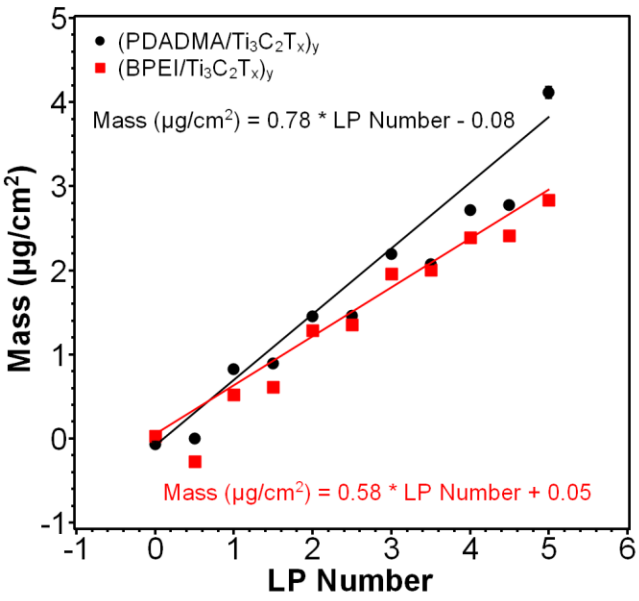

Figure 14. Composition of $Ti_3C_2T_x$ multilayers by QCM.

By measuring mass deposited every half layer pair, it is possible to calculate the wt% for both the polycation and MXene. From QCM, the wt% for $(PDADMA/Ti_3C_2T_x)_5$ was determined to be 5.5% PDADMA and 94.5% $Ti_3C_2T_x$. $(BPEI/Ti_3C_2T_x)_5$ was determined to be 9.3% BPEI and 90.7% $Ti_3C_2T_x$. This shows that the majority of the film is $Ti_3C_2T_x$ in both cases and confirms the assumption that layer growth is dominated by $Ti_3C_2T_x$. As the polymer content was not high enough to significantly mitigate oxidation considering the findings of Habib *et al.*, the additional need for an antioxidant to mitigate oxidation was supported.[46,49]

3.3. pH Response of Thin Films

3.3.1. Determination of pH Sensing Range

As mentioned previously, the response of the sensor in basic pH environments was not explored fully. This was due to the hastened oxidation of the sensors in basic environments. This can be seen in Figure 15 where the pH range tested spanned from pH 3 to pH 10.

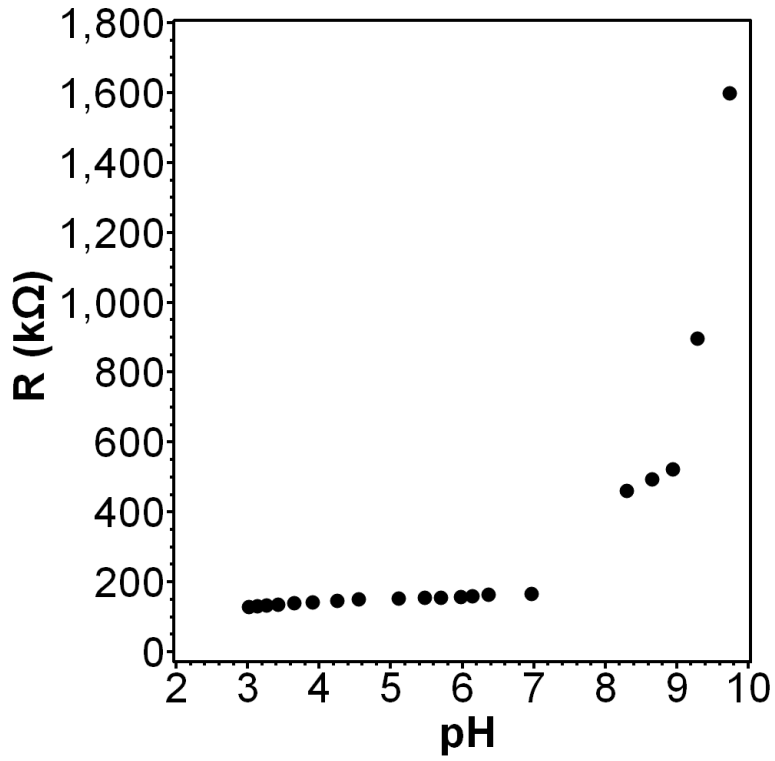

Figure 15. pH response of $(BPEI/Ti_3C_2T_x)_5$ from pH 3 to pH 10.

As can be seen in Figure 15, the resistance of the sensor exponentially increased after the film was exposed to basic conditions. However, the response in the acidic region was linear and a pH sensitivity for the sensor can be calculated to be 9.32 kΩ/pH or 7.32%/pH. The typical color change associated with oxidation (the film turning white due to the formation of TiO_2) can be seen in Figure 16 after sitting in basic conditions overnight.

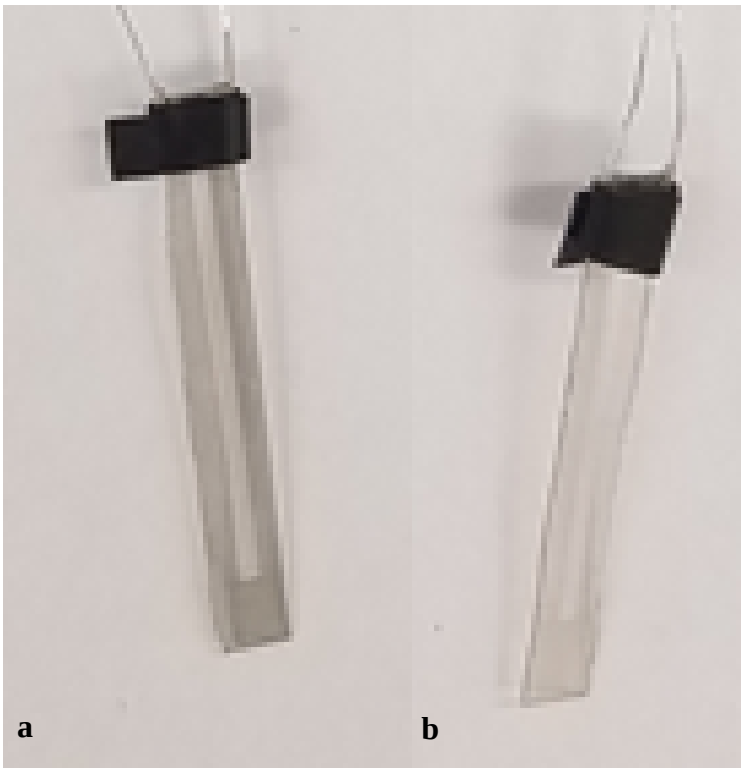

Figure 16. $(BPEI/Ti_3C_2T_x)_5$ sensor a) before and b) after extended range pH response testing.

The visible lightening in color of the film is indicative of the oxidation reaction of $Ti_3C_2T_x$ into TiO_2 which would explain the considerable increase in resistance associated with this experiment. As the drastic increase in resistance occurs above pH 7, the tested pH range was confined to acidic pH: pH 3 to pH 7.

3.3.2. (polycation/$Ti_3C_2T_x$) Thin Film Response

pH sensitivity of (PDADMA/$Ti_3C_2T_x$)$_5$ sensors were determined by exposing the sensor to environments of different pH ranging from pH 3 to pH 7 and recording the resistance. The figure of merit for the sensor, pH sensitivity, was quantified as the change in resistance per unit pH as well as the normalized change in resistance per unit pH. The latter was done to account for different loadings of $Ti_3C_2T_x$ and calculated as shown in Eq. 14.

$$\text{Sensitivity (\%)} = \frac{\Delta R}{R^o_{pH\ 3} * \Delta pH} \text{ x } 100 \qquad (14)$$

where ΔR is the change in resistance (kΩ), $R^o_{pH\ 3}$ is the resistance (kΩ) for the initial measurement at pH 3, and ΔpH is the change in pH.

A typical response plot for (PDADMA/$Ti_3C_2T_x$)$_5$ sensors can be seen in Figure 17 wherein resistance is plotted against pH.

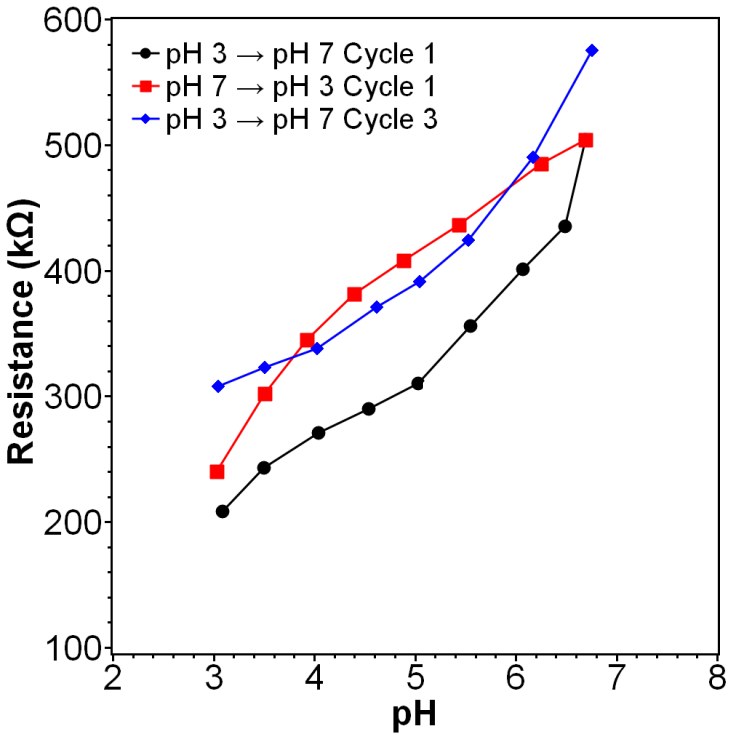

Figure 17. pH response of (PDADMA/$Ti_3C_2T_x$)$_5$. pH sensitivity of 23 kΩ/pH and 28 kΩ/pH for cycles 1 and 3, respectively.

Due to the noticeable hysteresis in the response depending on which direction pH was changing, the cycles were split into two segments: pH 3 → pH 7 and pH 7 → pH 3. pH 3 → pH 7 for cycles 1 and 3 were then compared to assess the cyclability of the sensors as shown in the inset. From the response plot, the pH sensitivity of the sensor can be quantified as the slope of the line of best fit for the data. This results in an initial pH sensitivity of 23 kΩ/pH (19.4 %/pH) for pH 3 → pH 7 Cycle 1 which increased to 28 kΩ/pH for pH 3 → pH 7 Cycle 3. However, there is overlap of the two cycles, indicating some degree of cyclability during the first few cycles. The response is attributed to the

(de)protonation of hydroxyl surface groups on the surface of the MXene. This leads to a change in the number of active charge carrier sites and electrostatic interaction between nanosheets. Both of which would lead to the corresponding changes in resistance. Change in electrostatic interaction leads to resistance changes as there will be intersheet attraction or repulsion that leads to changes in intersheet spacing. This is supported by the results of Natu *et al.* who observed a linear decrease in zeta potential with pH from pH 2 to pH 7.[50]

To determine the effect of adding a pH sensitive polymer, $(BPEI/Ti_3C_2T_x)_5$ sensors were tested as well (Figure 18).

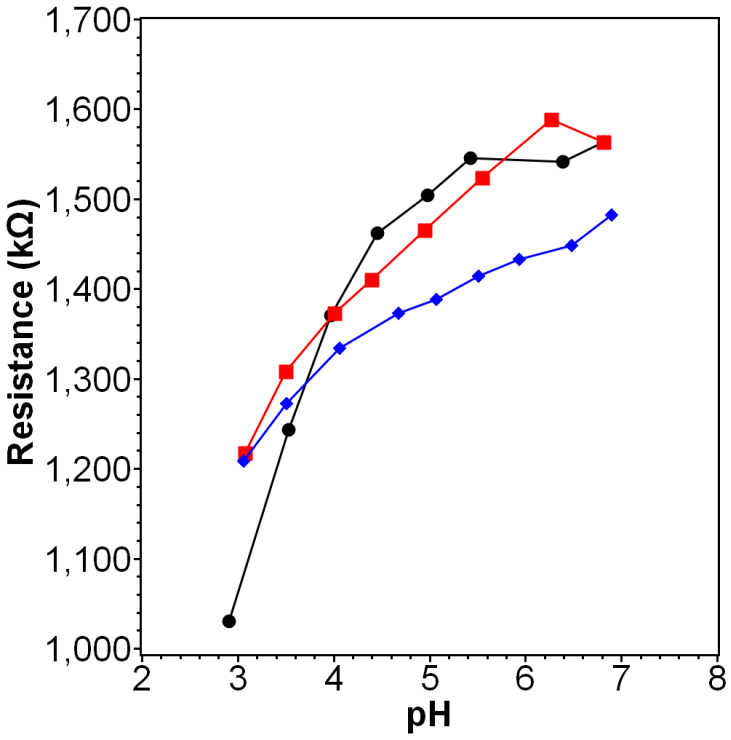

Figure 18. pH response of $(BPEI/Ti_3C_2T_x)_5$. pH sensitivity of 132 kΩ/pH and 141 kΩ/pH for cycles 1 and 3, respectively.

Once again, each cycle was split into two portions depending on which direction pH was changing. As compared to $(PDADMA/Ti_3C_2T_x)_5$ sensors, $(BPEI/Ti_3C_2T_x)_5$ sensors exhibited considerably higher pH sensitivities. In this case, the pH sensitivities were 132 kΩ/pH (68.1%/pH) for pH 3 → pH 7 Cycle 1 and 141 kΩ/pH for pH 3 → pH 7 Cycle 3. This increase can be attributed to the pH sensitivity of BPEI. As the pH of the solution the sensor is submerged in increases, the BPEI in the sensor deprotonates and causes the thickness of the sensor to increase and vice versa. The thickness change can be attributed to conformational changes of BPEI due to changes in electrostatic interactions caused by (de)protonation. The more positively charged deprotonated BPEI chains will have higher intrachain repulsion causing the polymer chains to straighten out. The straightened chains lead to lower thicknesses and subsequently sensor resistance. The resistance changes caused by BPEI compound with those from the MXene and result in enhanced pH sensitivity. Compared to other resistive sensors in Table 1, the LbL polycation/$Ti_3C_2T_x$ sensors exhibit considerably higher pH responsivities indicating that $Ti_3C_2T_x$ is highly pH sensitive. However, due to the poor oxidative stability of $Ti_3C_2T_x$, the pH sensing range is generally smaller as compared to other resistive sensors.[46,48]

To determine oxidative stability of the sensors, SEM and XPS characterization was done before and after pH response testing. SEM of the sensors is shown in Figure 19.

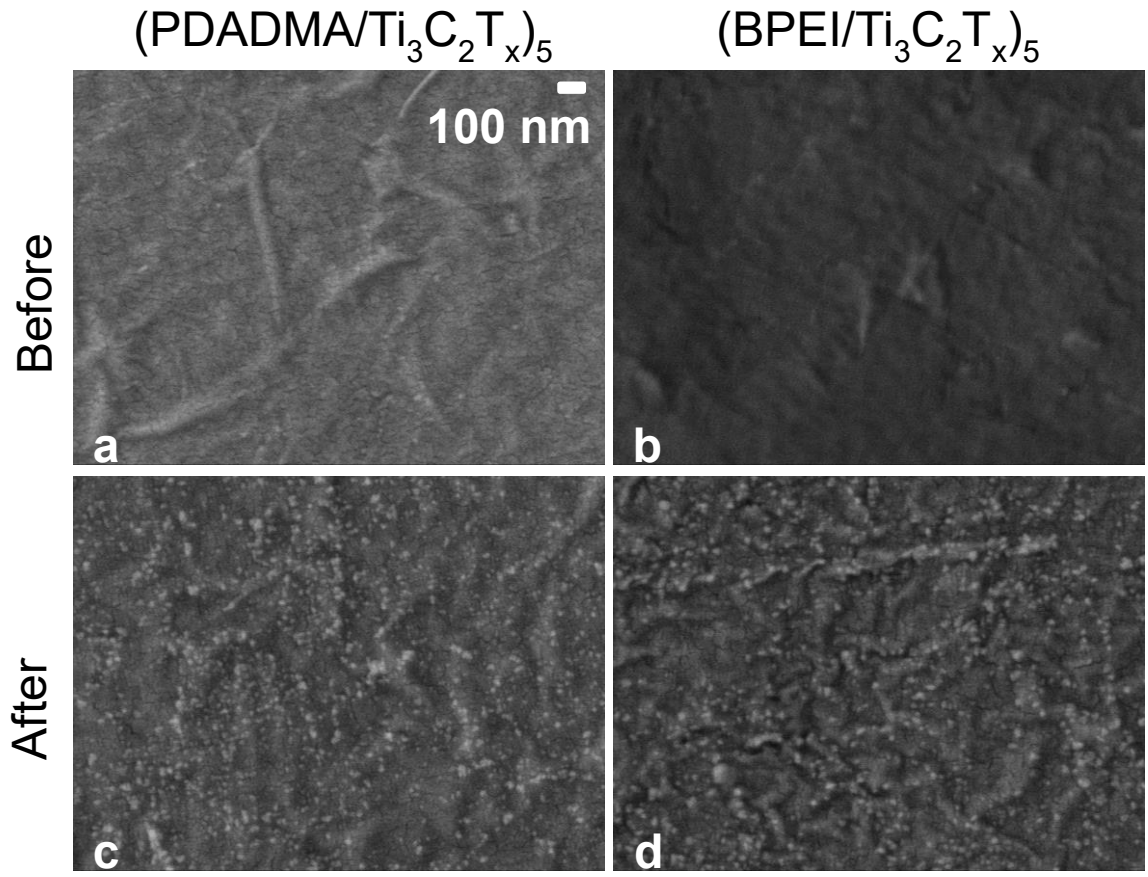

Figure 19. SEM of (a) $(PDADMA/Ti_3C_2T_x)_5$ and (b) $(BPEI/Ti_3C_2T_x)_5$ before and (c) $(PDADMA/Ti_3C_2T_x)_5$ and (d) $(BPEI/Ti_3C_2T_x)_5$ after pH response test.

After pH response testing, there are visible white particles that form after pH response testing for both sensors. Given that TiO_2 is white and that $Ti_3C_2T_x$ is known to be prone to oxidation, it is presumed that these flakes are TiO_2 and that the sensor has undergone oxidation during testing. This is confirmed using XPS to identify the change in components before and after testing.

As TiO_2 is the component of note, peak fittings for the Ti 2p spectra from XPS are first examined (Figure 20).

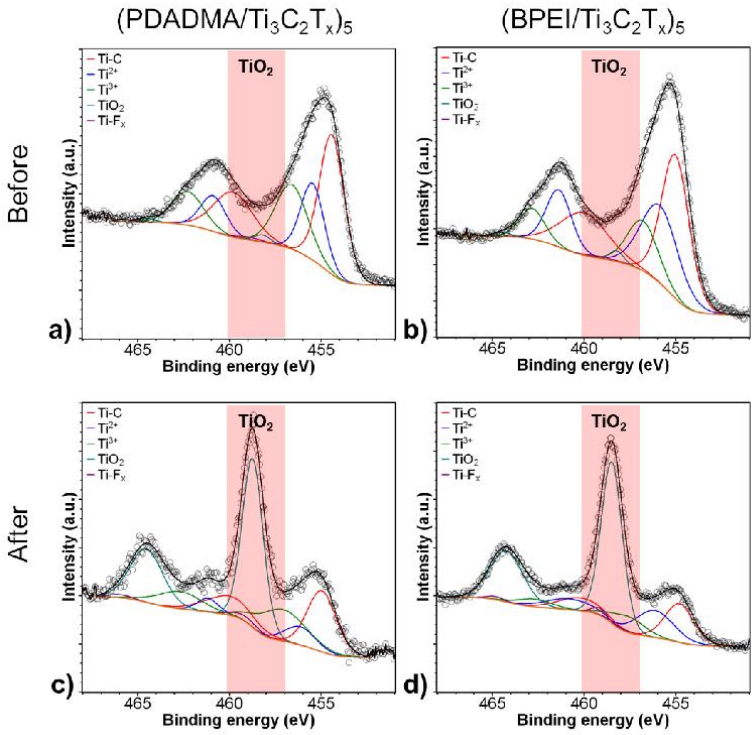

Figure 19. Deconvoluted Ti 2p XPS Spectra of (a) $(PDADMA/Ti_3C_2T_x)_5$ and (b) $(BPEI/Ti_3C_2T_x)_5$ films before and (c) $(PDADMA/Ti_3C_2T_x)_5$ and (d) $(BPEI/Ti_3C_2T_x)_5$ films after pH response test.

The TiO_2 peak typically occurs at ~459 and ~ 464 eV, and the former is labeled in Figure 20.[49] Before the pH response test, the TiO_2 peak is minimal for both sensor compositions. However, after testing TiO_2 dominates the Ti 2p spectra and forms a sharp peak. This is indicative of considerable oxidation of the film during testing. In both cases, the TiO_2

component AT% increases significantly from ~1% to ~50% (Tables 3-6). As in Table 2, the values in parentheses correspond to the Ti $2p_{1/2}$ orbital.

Table 3. XPS peak fitting results for (PDADMA/$Ti_3C_2T_x$)$_5$ before pH response test.

Element	Element at%	Binding energy (eV)	Component name	Component at%	FWHM
Ti 2p3/2 (2p1/2)	4.9	454.4 (459.8)	Ti-C	46.7	1.6 (2.5)
		455.5 (460.9)	Ti^{2+}	23.8	1.5 (1.6)
		456.6 (462.2)	Ti^{3+}	27.6	2.1 (2.0)
		458.2 (464.5)	TiO_2	1.5	1.0 (1.0)
		459.0 (465.8)	Ti-F_x	0.9	1.6 (1.0)
C 1s	77.6	281.0	C-Ti-T_x	4.9	1.2
		282.6	C-Ti-T_x	2.2	1.7
		284.8	C-C	78.6	1.8
		286.4	CH_x/CO	9.2	1.6
		287.6	C-OH	0.3	0.6
		288.6	COO	4.8	1.7
O 1s	15.4	529.2	TiO_2	20.0	1.9
		530.9	C-Ti-O_x	12.2	1.3
		531.9	C-Ti-$(OH)_x$	47.6	1.9
		533.3	Al_2O_3	16.1	2.0
		534.2	H_2O	4.2	3.0
F 1s	1.1	684.3	C-Ti-F_x	96.7	1.7
		686.0	AlF_x	3.3	1.0
Cl 2p	1.0	-	-	-	-

Table 4. XPS peak fitting results for $(BPEI/Ti_3C_2T_x)_5$ before pH response test.

Element	Element at%	Binding energy (eV)	Component name	Component at%	FWHM
Ti 2p3/2 (2p1/2)	7.3	455.0 (460.0)	Ti-C	46.3	1.8 (3.0)
		455.9 (461.4)	Ti^{2+}	33.5	2.4 (1.6)
		456.8 (462.8)	Ti^{3+}	17.9	2.0 (1.6)
		458.2 (464.5)	TiO_2	1.7	0.9 (1.2)
		459.1 (466.2)	Ti-F_x	0.6	1.9 (0.7)
C 1s	73.0	281.6	C-Ti-T_x	6.8	1.2
		283.1	C-Ti-T_x	7.0	3.0
		284.8	C-C	63.3	1.6
		286.0	CH_x/CO	19.2	2.3
		288.1	C-OH	1.6	1.3
		289.0	COO	2.0	1.2
O 1s	14.5	529.5	TiO_2	15.9	1.5
		530.9	C-Ti-O_x	25.3	2.9
		531.6	C-Ti-$(OH)_x$	36.4	1.7
		532.7	Al_2O_3	12.5	1.3
		533.7	H_2O	9.9	1.5
F 1s	1.8	684.8	C-Ti-F_x	93.1	1.8
		686.9	AlF_x	6.9	1.6
Cl 2p	1.3	-	-	-	-
N 1s	2.0	-	-	-	-

Table 5. XPS peak fitting results for (PDADMA/$Ti_3C_2T_x$)$_5$ after pH response test.

Element	Element at%	Binding energy (eV)	Component name	Component at%	FWHM
Ti 2p3/2 (2p1/2)	2.3	455.0 (460.0)	Ti-C	23.7	1.9 (3.0)
		456.1 (461.2)	Ti^{2+}	7.6	2.0 (1.3)
		457.1 (462.7)	Ti^{3+}	19.8	3.0 (2.8)
		458.7 (464.8)	TiO_2	47.1	1.3 (2.1)
		459.1 (466)	Ti-F_x	1.9	1.7 (1.4)
C 1s	77.7	281.5	C-Ti-T_x	1.5	1.5
		283.1	C-Ti-T_x	2.1	1.3
		284.8	C-C	79.8	1.6
		286.2	CH_x/CO	11.8	2.1
		288.2	COH	1.4	0.9
		288.9	COO	3.4	1.4
O 1s	19.0	530.0	TiO_2	14.2	1.6
		530.4	C-Ti-O_x	5.3	1.0
		531.7	C-Ti-$(OH)_x$	50.3	1.6
		532.7	Al_2O_3	13.0	1.2
		533.4	H_2O	17.3	1.8
F 1s	0.4	684.6	C-Ti-F_x	73.6	1.7
		686.4	AlF_x	26.4	1.9
Cl 2p	0.6	-	-	-	-

Table 6. XPS peak fitting results for $(BPEI/Ti_3C_2T_x)_5$ after pH response test.

Element	Element at%	Binding energy (eV)	Component name	Component at%	FWHM
Ti 2p3/2 (2p1/2)	3.7	454.8 (460.2)	Ti-C	18.1	1.9 (2.8)
		456.1 (460.8)	Ti^{2+}	16.6	2.4 (3.0)
		457.6 (462.7)	Ti^{3+}	8.6	2.1 (2.2)
		458.5 (464.2)	TiO_2	55.0	1.3 (2.1)
		459.2 (464.8)	$Ti\text{-}F_x$	1.7	0.9 (1.1)
C 1s	72.7	281.0	$C\text{-}Ti\text{-}T_x$	1.7	1.4
		283.2	$C\text{-}Ti\text{-}T_x$	2.7	1.8
		284.8	C-C	72.6	1.5
		286.2	CH_x/CO	12.1	1.4
		287.9	C-OH	7.6	2.6
		288.8	COO	3.3	1.2
O 1s	21.5	529.8	TiO_2	24.4	1.6
		530.9	$C\text{-}Ti\text{-}O_x$	12.2	1.4
		532.0	$C\text{-}Ti\text{-}(OH)_x$	44.5	1.6
		532.9	Al_2O_3	0.8	0.5
		533.4	H_2O	18.2	1.6
F 1s	0.5	684.3	$C\text{-}Ti\text{-}F_x$	26.9	0.8
		684.7	AlF_x	73.1	2.3
Cl 2p	0.4	-	-	-	-
N 1s	1.2	-	-	-	-

The peak fittings for the other components (C 1s, O 1s, and F 1s) are also examined to support the claim of oxidation. This is shown in Figure 21 for $(PDADMA/Ti_3C_2T_x)_5$ and Figure 22 for $(BPEI/Ti_3C_2T_x)_5$.

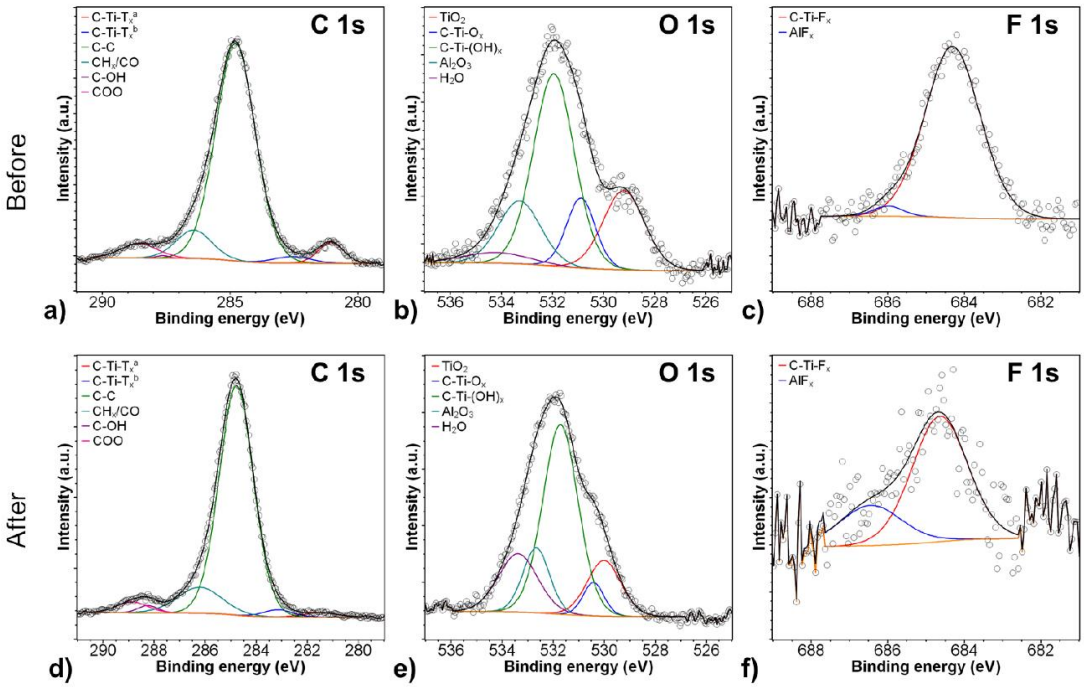

Figure 20. Deconvoluted XPS of (PDADMA/$Ti_3C_2T_x$)$_5$ for (a) C 1s, (b) O 1s, (c) F 1s before and (d) C 1s, (e) O 1s, (f) F 1s after pH response test.

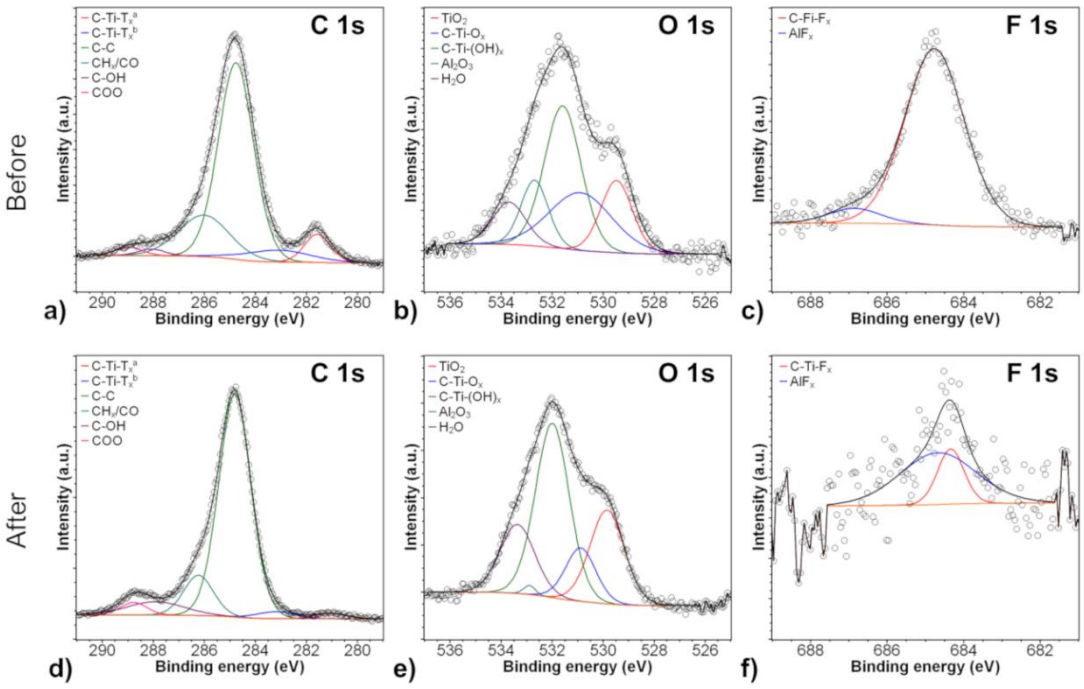

Figure 21. Deconvoluted XPS of (BPEI/$Ti_3C_2T_x$)$_5$ for (a) C 1s, (b) O 1s, (c) F 1s before and (d) C 1s, (e) O 1s, (f) F 1s after pH response test.

In the C 1s spectra, the two symmetric peaks representing the asymmetric C-Ti-T_x component drastically decreases after testing. Additionally, in the F 1s spectra the C-Ti-F_x peak drastically shrinks. Both of these changes support the claim that the sensors are oxidizing.

3.3.3. Response of (polycation/$Ti_3C_2T_x$) sensors without NaAsc treatment

To determine the effect of NaAsc, sensors prepared with untreated $Ti_3C_2T_x$ were tested as well as shown in Figure 23.

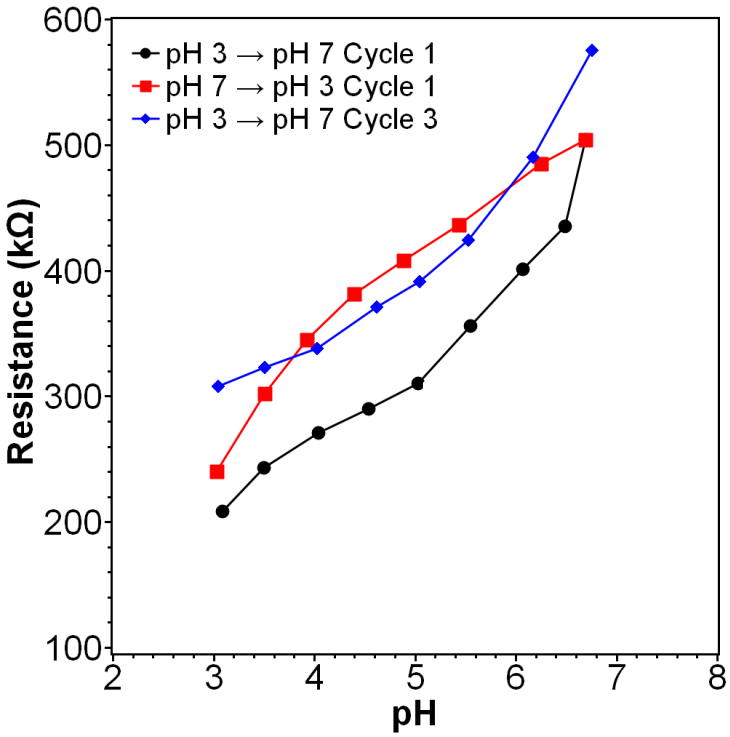

Figure 22. $(PDADMA/Ti_3C_2T_x)_5$ pH response. pH sensitivity of 72 kΩ/pH and 68 kΩ/pH for cycles 1 and 3, respectively. $Ti_3C_2T_x$ was not treated with NaAsc.

As compared to $(PDADMA/Ti_3C_2T_x)_5$ sensors treated with NaAsc, the untreated sensors display higher pH sensitivities (72 kΩ/pH for the untreated sensor vs. 28 kΩ/pH for the treated sensor). The higher sensitivity can be attributed to both the higher initial resistance of the untreated sensor as well as oxidation of the sensor. Normalizing for the initial resistance, the untreated sensor had a sensitivity of 34.6 %/pH vs. 19.4 %/pH for the treated counterpart. As oxidation would increase the resistance of the film, it would be additive to the change in resistance caused by the pH sensitivity of the sensor, leading to an artificially higher pH sensitivity. This claim is supported by the significantly higher

resistance at pH 3 for Cycle 1 and Cycle 3 and contributes to the higher normalized pH sensitivity. The higher initial resistance, almost double that of the NaAsc treated sensor, and noticeably worse cyclability lead to the conclusion that treatment with NaAsc is beneficial for sensor performance.

Films prepared with untreated $Ti_3C_2T_x$ were compared again for sensors made using BPEI. The response of a typical $(BPEI/Ti_3C_2T_x)_5$ sensor without NaAsc treatment can be seen in Figure 24.

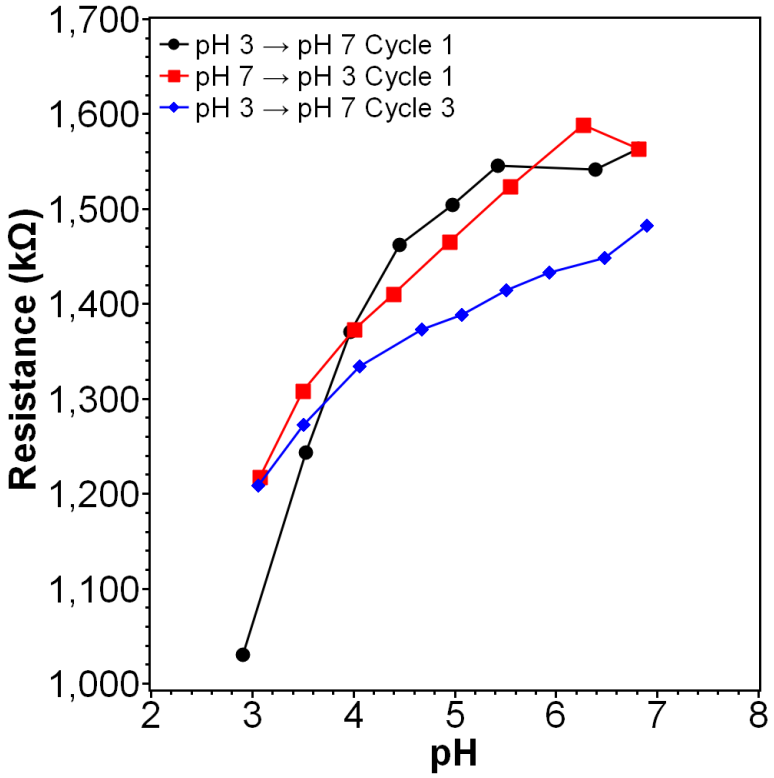

Figure 23. pH response of $(BPEI/Ti_3C_2T_x)_5$. pH sensitivity of 120 kΩ/pH and 65 kΩ/pH for cycles 1 and 3, respectively. $Ti_3C_2T_x$ was not treated with NaAsc for these tests.

As with the untreated (PDADMA/$Ti_3C_2T_x$)$_5$ sensor, the initial resistance for the untreated (BPEI/$Ti_3C_2T_x$)$_5$ sensor was considerably higher than its NaAsc treated counterpart. In this case, the initial resistance was an order of magnitude higher. While the pH sensitivities were similar in this case (120 kΩ/pH for untreated (BPEI/$Ti_3C_2T_x$)$_5$ vs. 132 kΩ/pH for (BPEI/$Ti_3C_2T_x$)$_5$ treated with NaAsc), the response was nonlinear and decreased considerably by the third cycle (120 kΩ/pH for Cycle 1 to 65 kΩ/pH for Cycle 3). The high sensitivity was also due in part to the higher resistance of the film. Comparing the normalized resistance change, the untreated film had a normalized pH sensitivity of 12 %/pH whereas the treated film had a normalized pH sensitivity of 68.1 %/pH. This confirms that NaAsc was beneficial to sensor performance.

3.4. Comparison to rGO Based Sensors

As with $Ti_3C_2T_x$ based films, growth profiles were obtained for rGO based sensors. All growth characterization was done prior to reduction of GO. This is due to the corrosive nature of HI and the discoloration of the substrates after reduction. Based on the results of De *et al.*, a ~5% reduction in thickness can be expected after reduction of the GO multilayers.[82] To compare the initial size of the nanomaterial, AFM was used to measure nanosheet thickness of GO (Figure 25).

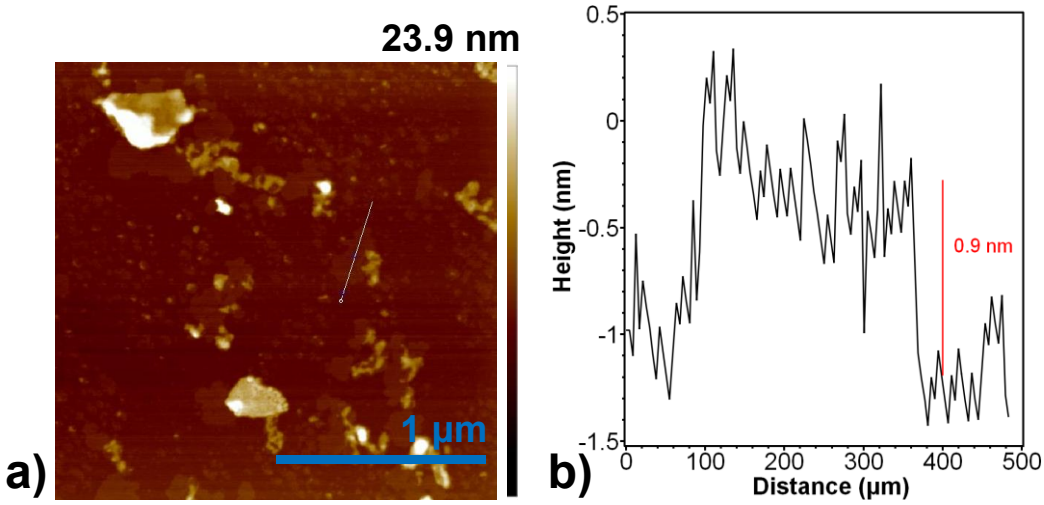

Figure 24. (a) AFM topographical scan and (b) height profile of survey scan of GO nanosheets.

From AFM, a typical nanosheet size of 0.9 nm and lateral size of 0.2 to 0.6 micron are obtained for GO (Figure 25). The thickness is similar to the monolayer nanosheet size obtained for $Ti_3C_2T_x$ (1 nm) whereas lateral size is considerably smaller. However, there is noticeable aggregation of the nanosheets.

After verifying nanosheet thickness, a growth profile with thickness and roughness of GO multilayers was obtained from profilometry as shown in Figure 26.

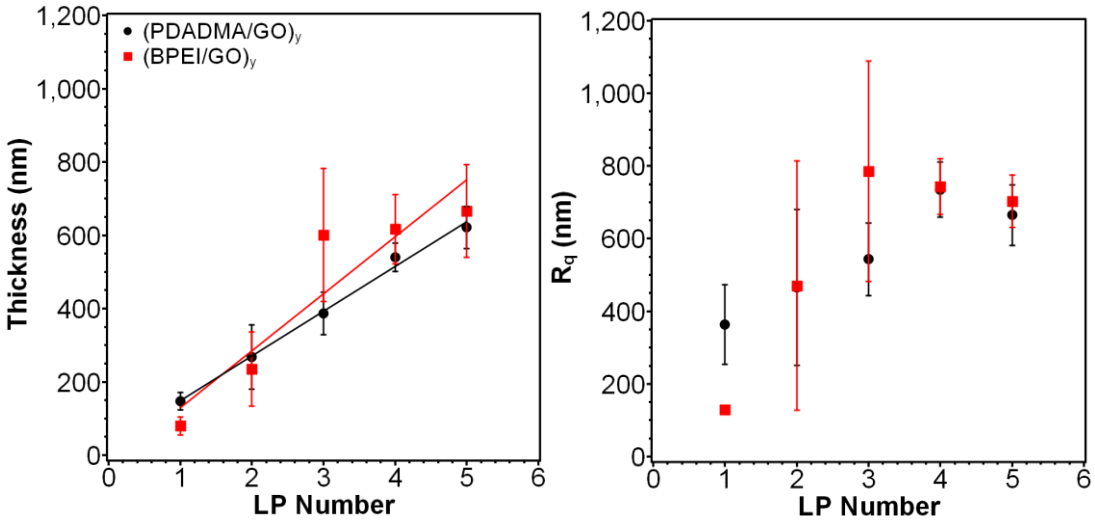

Figure 25. (a) Thickness and (b) RMS roughness of GO based multilayers as measured by profilometry. Thickness increases as 122 nm/LP and 155 nm/LP for $(PDADMA/GO)_y$ and $(BPEI/GO)_y$, respectively.

As opposed to $Ti_3C_2T_x$ multilayers, the thickness and roughness of GO multilayers is an order of magnitude larger with a layer growth of 122 nm and 155 nm per layer pair for films with PDADMA and BPEI, respectively. This higher rate of deposition can be attributed to aggregation of the GO nanosheets in dispersion and leads to a lower resistance of rGO based films as resistance is inversely related to thickness as shown in Eq. 15.

$$R = \frac{\rho l}{tw} \tag{15}$$

where R is resistance, ρ is resistivity, l is path length, t is film thickness, w is path width.

As before, thickness was verified using ellipsometry as shown in Figure 27.

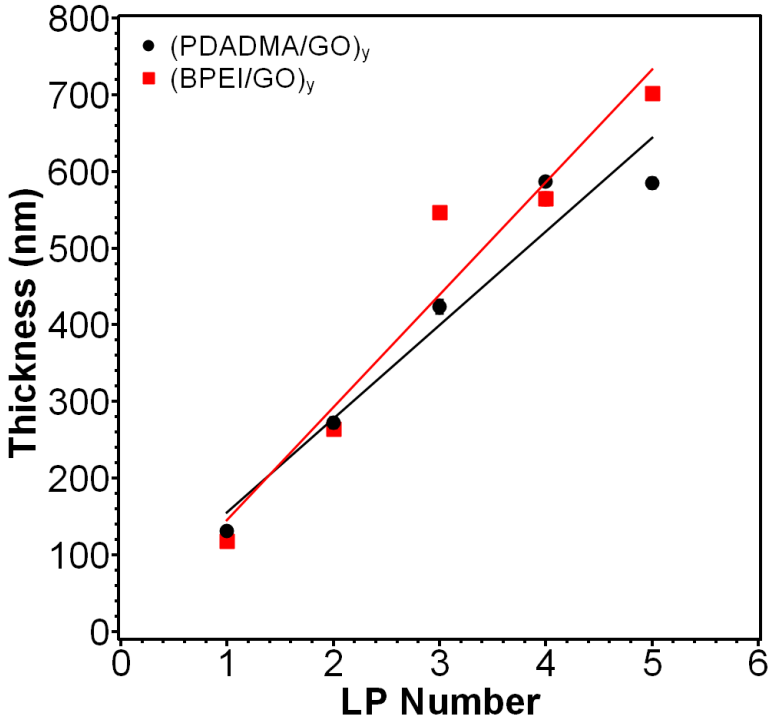

Figure 26. Thickness of GO based multilayers as determined by ellipsometry. Thickness increases as 122 nm/LP and 147 nm/LP for $(PDADMA/GO)_y$ and $(BPEI/GO)_y$, respectively.

From ellipsometry, layer growth was determined to be 122 nm and 147 nm per layer pair for $(PDADMA/GO)_y$ and $(BPEI/GO)_y$, respectively, which is in agreement with the results of profilometry. However, as thicknesses from profilometry were used for $Ti_3C_2T_x$ multilayers, they will be used for GO multilayers as well to maintain consistency.

Spectroscopy results of GO multilayers can be seen in Figure 28.

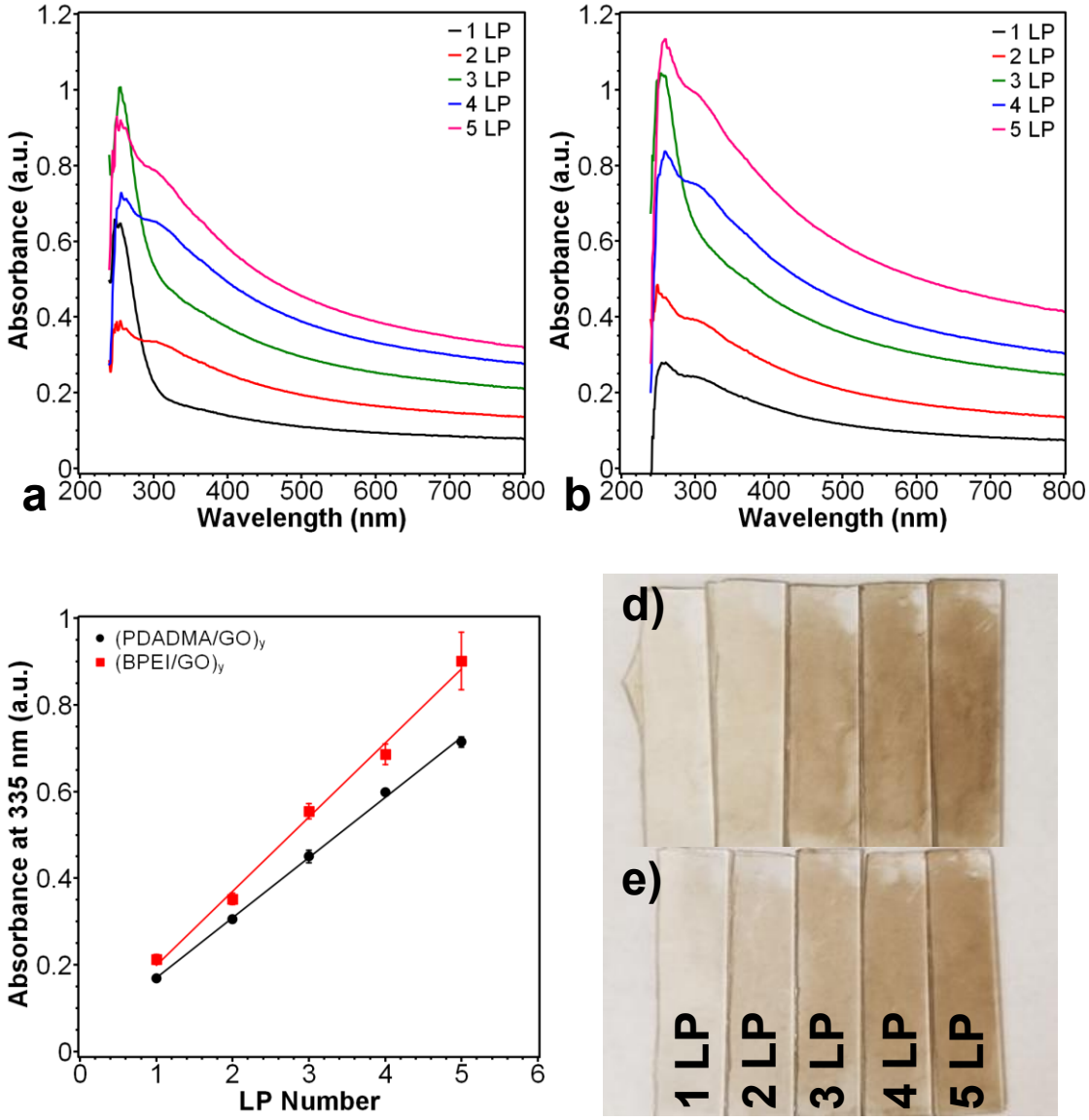

Figure 27. Absorbance of (a) $(PDADMA/GO)_y$, (b) $(BPEI/GO)_y$, and (c) GO multilayers at 335 nm as measured by spectrophotometry and digital images of (d) $(PDADMA/GO)_y$ and (e) $(BPEI/GO)_y$.

The absorbance increases at a rate of 0.14 a.u. and 0.17 a.u. per LP for $(PDADMA/GO)_y$ and $(BPEI/GO)_y$ respectively. The absorbance can once again be correlated with the

thickness as shown in Eq. 16 for $(PDADMA/GO)_y$ and Eq. 17 for $(BPEI/GO)_y$ respectively.

$$t \text{ (nm)} = 872 * \text{absorbance (a.u.)} - 3 \quad (16)$$

$$t \text{ (nm)} = 914 * \text{absorbance (a.u.)} - 54 \quad (17)$$

Polycation and GO content in the films was verified using QCM as shown in Figure 29.

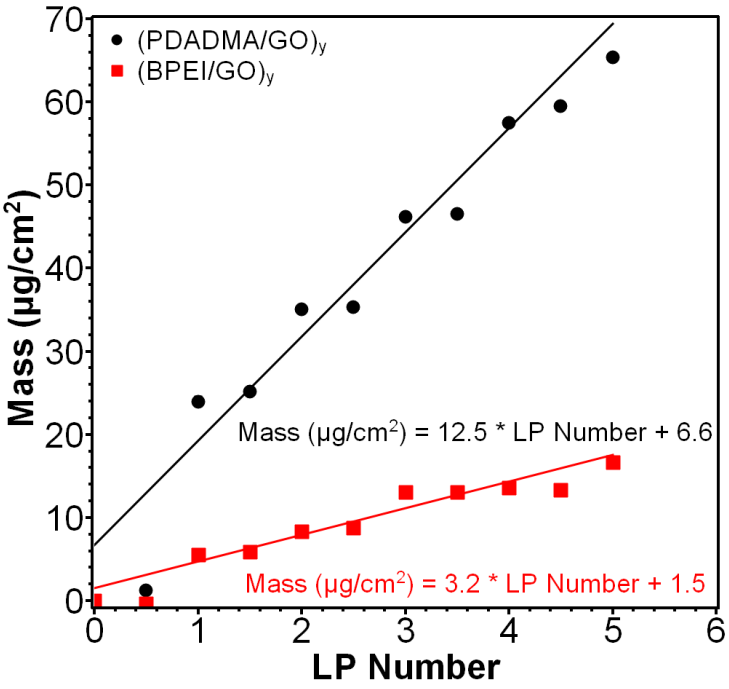

Figure 28. Composition of GO multilayers from QCM.

$(PDADMA/GO)_5$ contains 90.7% GO and 9.3% PDADMA and $(BPEI/GO)_5$ contains 92.2% GO and 7.8% BPEI. Similar to $Ti_3C_2T_x$ multilayers, the polycation makes up a minor part of the film by weight.

Once the layer growth was confirmed, the GO based multilayers were reduced to obtain the rGO based sensors. After reduction, the films noticeably change color as shown in Figure 30, and the resistance dropped considerably.

Figure 29. $(BPEI/GO)_5$ (a) before and (b) after reduction.

The color of the film changed from a light brown to a dark gray after HI vapor reduction. Additionally, the resistance was measured to be 0.85 kΩ at a 3 mm distance using a multimeter after reduction. Prior to reduction, the resistance was too high to be measured (> 200 MΩ). As both color and resistance change occurred, successful reduction was verified.

After rGO multilayers were successfully fabricated, they were then used for pH response testing. Due to the hydrophobic nature of rGO and the time reported by Zheng *et al.* it takes for GO membranes to swell, the swelling time was increased to a minimum of 72 hours.[102] pH response of $(PDADMA/rGO)_5$ is shown in Figure 31.

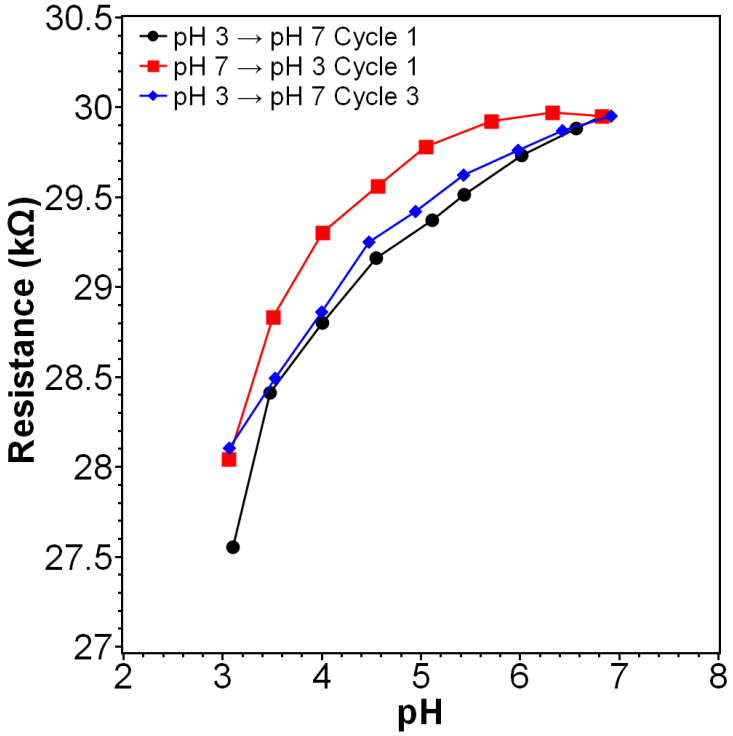

Figure 30. pH response of $(PDADMA/rGO)_5$. pH sensitivity of 0.6 kΩ/pH and 0.5 kΩ/pH for cycles 1 and 3, respectively.

As with $Ti_3C_2T_x$ based sensors, the pH was cycled 3 times from pH 3 → pH 7 → pH 3. The cycles were then split based off which direction pH was changing (pH 3 → pH 7 and

pH 7 → pH 3). As opposed to the treated $Ti_3C_2T_x$ sensors, $(PDADMA/rGO)_5$ had a significantly lower initial resistance and displayed a nonlinear response to pH. The lower initial resistance is due to the higher film thickness. When linearizing the pH response, the pH sensitivity of $(PDADMA/rGO)_5$ was estimated to be 0.6 kΩ/pH or 2.1 %/pH for pH 3 → pH 7 Cycle 1. Both of these sensitivities are considerably lower than what was observed for either composition of NaAsc treated $Ti_3C_2T_x$ based sensors. The lower sensitivity is attributed to the lack of surface functional groups of the rGO. As there are no surface sites to interact with H_3O^+ or OH^- ions in solution, the typical mechanism for pH response of graphenic materials such as graphene is not possible, and the sensor is expected to not be pH responsive.[62] However, there can be defects introduced during etching that allow for some pH response.

The pH sensitivity of $(BPEI/rGO)_5$ was also evaluated to provide a better comparison between $Ti_3C_2T_x$ and rGO based sensors (Figure 32).

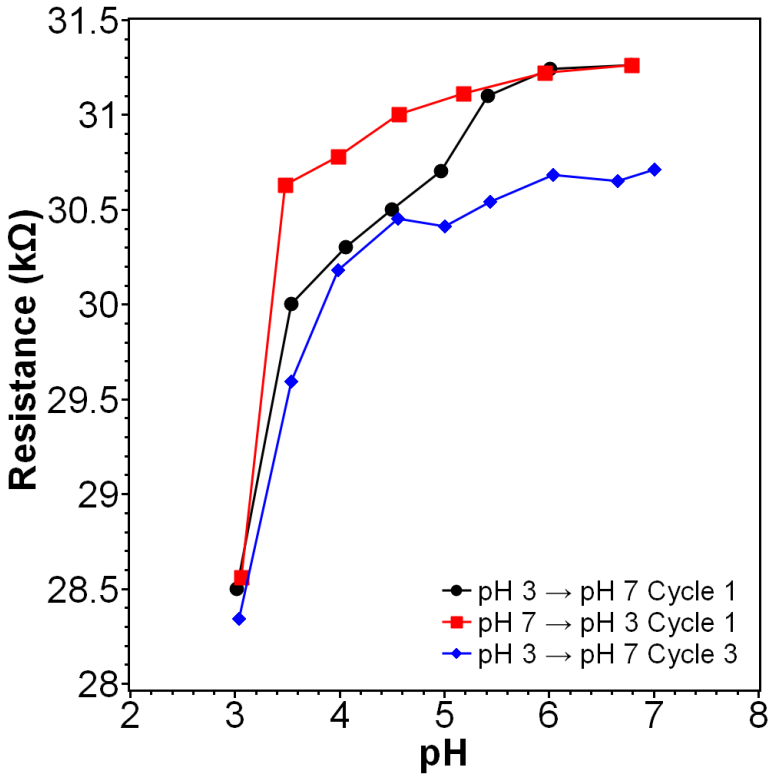

Figure 31. pH response of $(BPEI/rGO)_5$. pH sensitivity of 0.6 kΩ/pH and 0.5 kΩ/pH for cycles 1 and 3, respectively.

As with $(PDADMA/rGO)_5$, the initial resistance was an order of magnitude lower than that of the $Ti_3C_2T_x$ counterpart and the pH response was nonlinear. As before, the pH response was linearized to obtain an estimate of pH sensitivity. For the $(BPEI/rGO)_5$ sensors, the pH sensitivity was found to be 0.6 kΩ/pH or 2.1 %/pH for pH 3 → pH 7 Cycle 1 which was similar to the sensitivity of $(PDADMA/rGO)_5$. The low pH sensitivity is attributed to the same reasoning as for the $(PDADMA/rGO)_5$ sensor. Considering the differences in pH sensitivity, the $Ti_3C_2T_x$ sensors significantly outperform the rGO based sensors.

3.5. Comparison to Spray Assembled $Ti_3C_2T_x$ Sensor

Thickness and roughness of spray assembled $Ti_3C_2T_x$ sensors was 97.8 ± 57.8 nm and 47 ± 14.8 nm respectively. The thickness was approximately double that of the LbL assembled $(PDADMA/Ti_3C_2T_x)_5$ sensors, and the roughness was significantly higher. This increase in thickness and roughness can be attributed to the less controllable assembly method. Additionally, as there was no polymer to improve the adhesive properties of the $Ti_3C_2T_x$, the thin film was prone to peeling off with tape as shown in Figure 33.

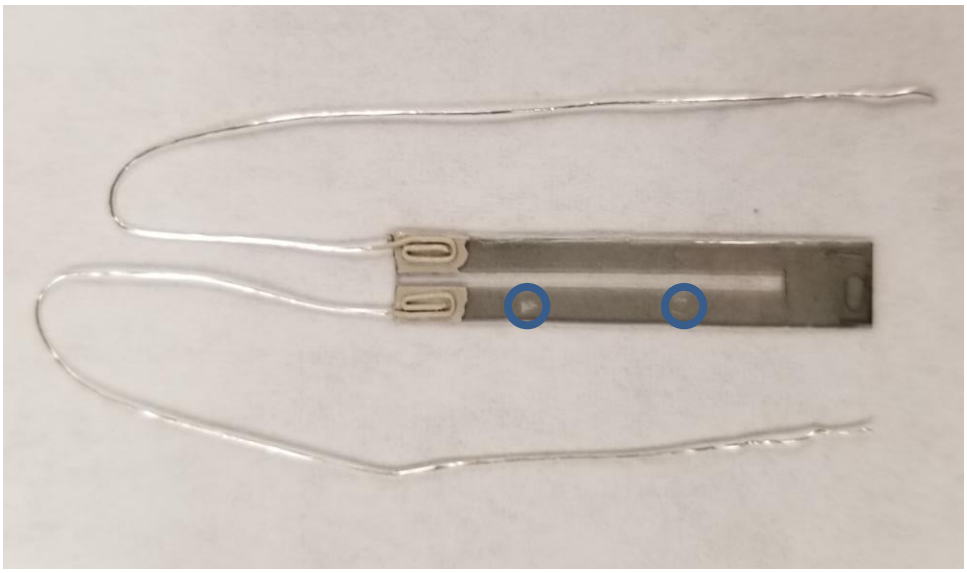

Figure 32. Spray assembled $Ti_3C_2T_x$ sensor.

This issue was observed previously by An *et al.* albeit for a drop cast $Ti3C_2T_x$ film.[64] The delamination of the $Ti_3C_2T_x$ film leads to destruction of the conductive pathway as the

delaminated section would no longer be conductive. This makes it difficult to produce consistent and repeatable sensors via this method despite being able to make these films on a larger scale. As such, these sensors were not compared to the LbL polycation/$Ti_3C_2T_x$ sensors.

3.6. Comparison to Resistive Sensors in Literature

The response of $Ti_3C_2T_x$ and rGO based multilayers fabricated in this work was then compared to other resistive sensors as shown in Table 7.

Table 7. Comparison of pH Range and Sensitivity for Resistive Sensors in Literature.

Material	pH Sensitivity	pH Range	Reference
SWNT-PANI/PVA	20 kΩ/cm^2/pH	1 – 10	77
p-SWNT-PSS/PANI	4.56 kΩ/cm^2/pH acidic region 20.66 kΩ/cm^2/pH basic region	0.95 – 12	54
Graphene	2 kΩ/pH	4 – 10	63
MWNT	65 Ω/pH	5 – 9	78
Pd	5 %/pH	4 – 10	80
MWCNT/Ni	1 %/pH	2 – 10	81
ES-PANI/PVB	0.28 MΩ/pH	1 – 8	79
$(PDADMA/rGO)_5$	0.6 kΩ/pH	3 – 7	This work
$(BPEI/rGO)_5$	0.6 kΩ/pH	3 – 7	This work
$(PDADMA/Ti_3C_2T_x)_5$	23 kΩ/pH 48 kΩ/cm^2/pH 19.4 %/pH	3 – 7	This work
$(BPEI/Ti_3C_2T_x)_5$	132 kΩ/pH 228 kΩ/cm^2/pH 68.1 %/pH	3 – 7	This work

As compared to other resistive sensors in literature, $Ti_3C_2T_x$ based sensors were confined to a smaller pH range due to the hastened oxidation of $Ti_3C_2T_x$ in basic conditions.[103]

However, with the exception of ES-PANI/PVB resistive sensors, $Ti_3C_2T_x$ based sensors exhibited considerably higher pH sensitivities as compared to other resistive sensors in literature. For the ES-PANI/PVB sensor, the response was nonlinear which makes it difficult to compare to our work as the response verifies depending on what pH range is being examined.

The higher sensitivity of $Ti_3C_2T_x$ based sensors is attributed to the hydroxyl surface groups. As the proposed mechanism of pH sensing for graphenic materials relies on the interaction of H_3O^+ and OH^- ions with the surface of the material, it is expected that having more active surface sites corresponds with higher sensitivities.[62] Additionally, Cai *et al*. has demonstrated that using LbL assembly results in better sensor performance as compared to other assembly methods due to the ordered structure obtained with LbL assembly.[65] Due to these factors, it is expected that LbL assembled $Ti_3C_2T_x$ based films will exhibit higher pH sensitivities, which was confirmed experimentally in this work.

4. SUMMARY AND FUTURE WORK

4.1. Summary

Herein, we have demonstrated the successful etching and processing of MAX phase powder to MXene nanosheets: Ti_3AlC_2 to $Ti_3C_2T_x$. Etching was verified with a variety of techniques including XRD, XPS, and SEM. The as produced nanosheets were then successfully used in the fabrication of nanometer scale thin films with uniform and well-defined layers. These multilayer films were subjected to pH response testing and showed, for the most part, a linear correlation of pH and film resistance. However, the response of the multilayers decreased throughout response testing, leading to the multilayers being considered single or few use due to their poor robustness. This robustness can be attributed to the behavior of $Ti_3C_2T_x$ at extreme pH (e.g. acid induced crumpling of $Ti_3C_2T_x$ in dispersion) and the increased rate of oxidation caused by full submersion of the multilayers in water for extended periods (24 hours of swelling in addition to the duration of the experiment).[51] Despite the poor robustness of the film, the multilayers possess an extremely high sensitivity, outperforming that of other resistive pH sensors in literature.[54,63,77,78,80,81]

4.2. Future Work

Future work pertains to the application of $Ti_3C_2T_x$ multilayers in sensing other environmental stimuli. One such application currently being explored is gas sensing. Due to the high surface area to volume ratio of $Ti_3C_2T_x$ and surface functional hydroxyl groups, it is an ideal material for gas sensing. The target analyte molecules can readily diffuse

through the LbL assembled $Ti_3C_2T_x$ multilayers and adsorb to the hydroxyl groups. The adsorption reduces the available number of charge carrier sites available which subsequently leads to increases in resistance. While there are existing $Ti_3C_2T_x$ based gas sensors, we expect our assembly procedure to enhance the response of the film as the layered structure would facilitate diffusion by improving porosity of the multilayers and make adsorption sites more readily accessible.[36,66,104] Additionally, we aim to explore the LbL assembly of films using other MXenes such as Nb_2CT_x, V_2CT_x, and Ti_2CT_x and assess the properties of the prepared films.

REFERENCES

1 Naguib, M., Kurtoglu, M., Presser, V., Lu, J., Niu, J. *et al.* Two-Dimensional Nanocrystals Produced by Exfoliation of Ti3AlC2. *Adv. Mater.* **23**, 4248-4253, doi:10.1002/adma.201102306 (2011).

2 Naguib, M., Mochalin, V. N., Barsoum, M. W. & Gogotsi, Y. 25th Anniversary Article: MXenes: A New Family of Two-Dimensional Materials. *Adv. Mater.* **26**, 992-1005, doi:10.1002/adma.201304138 (2014).

3 Ghidiu, M., Lukatskaya, M. R., Zhao, M.-Q., Gogotsi, Y. & Barsoum, M. W. Conductive two-dimensional titanium carbide 'clay' with high volumetric capacitance. *Nature* **516**, 78, doi:10.1038/nature13970 (2014).

4 Naguib, M., Mashtalir, O., Carle, J., Presser, V., Lu, J. *et al.* Two-Dimensional Transition Metal Carbides. *ACS Nano* **6**, 1322-1331, doi:10.1021/nn204153h (2012).

5 Alhabeb, M., Maleski, K., Anasori, B., Lelyukh, P., Clark, L. *et al.* Guidelines for Synthesis and Processing of Two-Dimensional Titanium Carbide (Ti3C2Tx MXene). *Chem. Mater.* **29**, 7633-7644, doi:10.1021/acs.chemmater.7b02847 (2017).

6 Lakhe, P., Prehn, E. M., Habib, T., Lutkenhaus, J. L., Radovic, M. *et al.* Process Safety Analysis for Ti3C2Tx MXene Synthesis and Processing. *Ind. Eng. Chem. Res.* **58**, 1570-1579, doi:10.1021/acs.iecr.8b05416 (2019).

7 Dong, Y., Mallineni, S. S. K., Maleski, K., Behlow, H., Mochalin, V. N. *et al.* Metallic MXenes: A new family of materials for flexible triboelectric nanogenerators. *Nano Energy* **44**, 103-110, doi:https://doi.org/10.1016/j.nanoen.2017.11.044 (2018).

8 Lipatov, A., Alhabeb, M., Lukatskaya, M. R., Boson, A., Gogotsi, Y. *et al.* Effect of Synthesis on Quality, Electronic Properties and Environmental Stability of Individual Monolayer Ti3C2 MXene Flakes. *Advanced Electronic Materials* **2**, 1600255, doi:10.1002/aelm.201600255 (2016).

9 Tang, H., Hu, Q., Zheng, M., Chi, Y., Qin, X. *et al.* MXene–2D layered electrode materials for energy storage. *Progress in Natural Science: Materials International* **28**, 133-147, doi:https://doi.org/10.1016/j.pnsc.2018.03.003 (2018).

10 Halim, J., Lukatskaya, M. R., Cook, K. M., Lu, J., Smith, C. R. *et al.* Transparent Conductive Two-Dimensional Titanium Carbide Epitaxial Thin Films. *Chem. Mater.* **26**, 2374-2381, doi:10.1021/cm500641a (2014).

11 VahidMohammadi, A., Mojtabavi, M., Caffrey, N. M., Wanunu, M. & Beidaghi, M. Assembling 2D MXenes into Highly Stable Pseudocapacitive Electrodes with High Power and Energy Densities. *Adv. Mater.* **31**, 1806931, doi:10.1002/adma.201806931 (2019).

12 Han, F., Luo, S., Xie, L., Zhu, J., Wei, W. *et al.* Boosting the Yield of MXene 2D Sheets via a Facile Hydrothermal-Assisted Intercalation. *ACS Appl. Mater. Interfaces* **11**, 8443-8452, doi:10.1021/acsami.8b22339 (2019).

13 Rakhi, R. B., Ahmed, B., Hedhili, M. N., Anjum, D. H. & Alshareef, H. N. Effect of Postetch Annealing Gas Composition on the Structural and Electrochemical Properties of Ti2CTx MXene Electrodes for Supercapacitor Applications. *Chem. Mater.* **27**, 5314-5323, doi:10.1021/acs.chemmater.5b01623 (2015).

14 Ghidiu, M., Kota, S., Halim, J., Sherwood, A. W., Nedfors, N. *et al.* Alkylammonium Cation Intercalation into Ti3C2 (MXene): Effects on Properties and Ion-Exchange Capacity Estimation. *Chem. Mater.* **29**, 1099-1106, doi:10.1021/acs.chemmater.6b04234 (2017).

15 Osti, N. C., Naguib, M., Ganeshan, K., Shin, Y. K., Ostadhossein, A. *et al.* Influence of metal ions intercalation on the vibrational dynamics of water confined between MXene layers. *Physical Review Materials* **1**, 065406, doi:10.1103/PhysRevMaterials.1.065406 (2017).

16 Gao, Q., Come, J., Naguib, M., Jesse, S., Gogotsi, Y. *et al.* Synergetic effects of K+ and Mg2+ ion intercalation on the electrochemical and actuation properties of the two-dimensional Ti3C2 MXene. *Faraday Discuss.* **199**, 393-403, doi:10.1039/C6FD00251J (2017).

17 Xie, Y. & Kent, P. R. C. Hybrid density functional study of structural and electronic properties of functionalized Ti${}_{n+1}{X}_{n}$ ($X=\mathrm{C}$, N) monolayers. *PhRvB* **87**, 235441, doi:10.1103/PhysRevB.87.235441 (2013).

18 Halim, J. *Synthesis and transport properties of 2D transition metal carbides (MXenes)*, (2018).

19 Hart, J. L., Hantanasirisakul, K., Lang, A. C., Anasori, B., Pinto, D. *et al.* Control of MXenes' electronic properties through termination and intercalation. *Nat. Commun.* **10**, 522, doi:10.1038/s41467-018-08169-8 (2019).

20 Sang, X., Xie, Y., Lin, M.-W., Alhabeb, M., Van Aken, K. L. *et al.* Atomic Defects in Monolayer Titanium Carbide (Ti3C2Tx) MXene. *ACS Nano* **10**, 9193-9200, doi:10.1021/acsnano.6b05240 (2016).

21 Yang, S., Zhang, P., Wang, F., Ricciardulli, A. G., Lohe, M. R. *et al.* Fluoride-Free Synthesis of Two-Dimensional Titanium Carbide (MXene) Using A Binary Aqueous System. *Angew. Chem. Int. Ed.* **57**, 15491-15495, doi:10.1002/anie.201809662 (2018).

22 Ling, Z., Ren, C. E., Zhao, M.-Q., Yang, J., Giammarco, J. M. *et al.* Flexible and conductive MXene films and nanocomposites with high capacitance. *Proceedings of the National Academy of Sciences* **111**, 16676-16681, doi:10.1073/pnas.1414215111 (2014).

23 Naguib, M., Come, J., Dyatkin, B., Presser, V., Taberna, P.-L. *et al.* MXene: a promising transition metal carbide anode for lithium-ion batteries. *Electrochem. Commun.* **16**, 61-64, doi:https://doi.org/10.1016/j.elecom.2012.01.002 (2012).

24 Lukatskaya, M. R., Mashtalir, O., Ren, C. E., Dall'Agnese, Y., Rozier, P. *et al.* Cation Intercalation and High Volumetric Capacitance of Two-Dimensional Titanium Carbide. *Science* **341**, 1502-1505, doi:10.1126/science.1241488 (2013).

25 Chang, T.-H., Zhang, T., Yang, H., Li, K., Tian, Y. *et al.* Controlled Crumpling of Two-Dimensional Titanium Carbide (MXene) for Highly Stretchable, Bendable, Efficient Supercapacitors. *ACS Nano* **12**, 8048-8059, doi:10.1021/acsnano.8b02908 (2018).

26 Yang, L., Zheng, W., Zhang, P., Chen, J., Tian, W. B. *et al.* MXene/CNTs films prepared by electrophoretic deposition for supercapacitor electrodes. *J. Electroanal. Chem.* **830-831**, 1-6, doi:https://doi.org/10.1016/j.jelechem.2018.10.024 (2018).

27 Wang, L., Yuan, L., Chen, K., Zhang, Y., Deng, Q. *et al.* Loading Actinides in Multilayered Structures for Nuclear Waste Treatment: The First Case Study of Uranium Capture with Vanadium Carbide MXene. *ACS Appl. Mater. Interfaces* **8**, 16396-16403, doi:10.1021/acsami.6b02989 (2016).

28 Zhang, Y.-J., Zhou, Z.-J., Lan, J.-H., Ge, C.-C., Chai, Z.-F. *et al.* Theoretical insights into the uranyl adsorption behavior on vanadium carbide MXene. *ApSS* **426**, 572-578, doi:https://doi.org/10.1016/j.apsusc.2017.07.227 (2017).

29 Li, K., Zou, G., Jiao, T., Xing, R., Zhang, L. *et al.* Self-assembled MXene-based nanocomposites via layer-by-layer strategy for elevated adsorption capacities. *Colloids Surf. Physicochem. Eng. Aspects* **553**, 105-113, doi:https://doi.org/10.1016/j.colsurfa.2018.05.044 (2018).

30 Gao, G., O'Mullane, A. P. & Du, A. 2D MXenes: A New Family of Promising Catalysts for the Hydrogen Evolution Reaction. *ACS Catalysis* **7**, 494-500, doi:10.1021/acscatal.6b02754 (2017).

31 Ran, J., Gao, G., Li, F.-T., Ma, T.-Y., Du, A. *et al.* Ti3C2 MXene co-catalyst on metal sulfide photo-absorbers for enhanced visible-light photocatalytic hydrogen production. *Nat. Commun.* **8**, 13907, doi:10.1038/ncomms13907 (2017).

32 Seh, Z. W., Fredrickson, K. D., Anasori, B., Kibsgaard, J., Strickler, A. L. *et al.* Two-Dimensional Molybdenum Carbide (MXene) as an Efficient Electrocatalyst for Hydrogen Evolution. *ACS Energy Lett.* **1**, 589-594, doi:10.1021/acsenergylett.6b00247 (2016).

33 Ma, T. Y., Cao, J. L., Jaroniec, M. & Qiao, S. Z. Interacting Carbon Nitride and Titanium Carbide Nanosheets for High-Performance Oxygen Evolution. *Angew. Chem. Int. Ed.* **55**, 1138-1142, doi:10.1002/anie.201509758 (2016).

34 Zhao, L., Dong, B., Li, S., Zhou, L., Lai, L. *et al.* Interdiffusion Reaction-Assisted Hybridization of Two-Dimensional Metal–Organic Frameworks and Ti3C2Tx Nanosheets for Electrocatalytic Oxygen Evolution. *ACS Nano* **11**, 5800-5807, doi:10.1021/acsnano.7b01409 (2017).

35 Ma, S., Yuan, D., Jiao, Z., Wang, T. & Dai, X. Monolayer Sc2CO2: A Promising Candidate as a SO2 Gas Sensor or Capturer. *J. Phys. Chem. C* **121**, 24077-24084, doi:10.1021/acs.jpcc.7b07921 (2017).

36 Kim, S. J., Koh, H.-J., Ren, C. E., Kwon, O., Maleski, K. *et al.* Metallic Ti3C2Tx MXene Gas Sensors with Ultrahigh Signal-to-Noise Ratio. *ACS Nano* **12**, 986-993, doi:10.1021/acsnano.7b07460 (2018).

37 Xiao, B., Li, Y.-c., Yu, X.-f. & Cheng, J.-b. MXenes: Reusable materials for NH3 sensor or capturer by controlling the charge injection. *Sensors Actuators B: Chem.* **235**, 103-109, doi:https://doi.org/10.1016/j.snb.2016.05.062 (2016).

38 Yu, X.-f., Li, Y.-c., Cheng, J.-b., Liu, Z.-b., Li, Q.-z. *et al.* Monolayer Ti2CO2: A Promising Candidate for NH3 Sensor or Capturer with High Sensitivity and Selectivity. *ACS Appl. Mater. Interfaces* **7**, 13707-13713, doi:10.1021/acsami.5b03737 (2015).

39 Chen, X., Sun, X., Xu, W., Pan, G., Zhou, D. *et al.* Ratiometric photoluminescence sensing based on Ti3C2 MXene quantum dots as an intracellular pH sensor. *Nanoscale* **10**, 1111-1118, doi:10.1039/C7NR06958H (2018).

40 An, H., Habib, T., Shah, S., Gao, H., Patel, A. *et al.* Water Sorption in MXene/Polyelectrolyte Multilayers for Ultrafast Humidity Sensing. *ACS Appl. Nano. Mater.* **2**, 948-955, doi:10.1021/acsanm.8b02265 (2019).

41 Rakhi, R. B., Nayak, P., Xia, C. & Alshareef, H. N. Novel amperometric glucose biosensor based on MXene nanocomposite. *Sci. Rep.* **6**, 36422, doi:10.1038/srep36422 (2016).

42 Rasheed, P. A., Pandey, R. P., Rasool, K. & Mahmoud, K. A. Ultra-sensitive electrocatalytic detection of bromate in drinking water based on Nafion/Ti3C2Tx (MXene) modified glassy carbon electrode. *Sensors Actuators B: Chem.* **265**, 652-659, doi:https://doi.org/10.1016/j.snb.2018.03.103 (2018).

43 Zheng, J., Wang, B., Ding, A., Weng, B. & Chen, J. Synthesis of MXene/DNA/Pd/Pt nanocomposite for sensitive detection of dopamine. *J. Electroanal. Chem.* **816**, 189-194, doi:https://doi.org/10.1016/j.jelechem.2018.03.056 (2018).

44 Desai, M. L., Basu, H., Singhal, R. K., Saha, S. & Kailasa, S. K. Ultra-small two dimensional MXene nanosheets for selective and sensitive fluorescence detection of Ag+ and Mn2+ ions. *Colloids Surf. Physicochem. Eng. Aspects* **565**, 70-77, doi:https://doi.org/10.1016/j.colsurfa.2018.12.051 (2019).

45 Peng, X., Zhang, Y., Lu, D., Guo, Y. & Guo, S. Ultrathin Ti3C2 nanosheets based "off-on" fluorescent nanoprobe for rapid and sensitive detection of HPV infection. *Sensors Actuators B: Chem.* **286**, 222-229, doi:https://doi.org/10.1016/j.snb.2019.01.158 (2019).

46 Habib, T., Zhao, X., Shah, S. A., Chen, Y., Sun, W. *et al.* Oxidation stability of Ti3C2Tx MXene nanosheets in solvents and composite films. *npj 2D Materials and Applications* **3**, 8, doi:10.1038/s41699-019-0089-3 (2019).

47 Lotfi, R., Naguib, M., Yilmaz, D. E., Nanda, J. & van Duin, A. C. T. A comparative study on the oxidation of two-dimensional Ti3C2 MXene structures in different environments. *J. Mater. Chem. A* **6**, 12733-12743, doi:10.1039/C8TA01468J (2018).

48 Zhang, C. J., Pinilla, S., McEvoy, N., Cullen, C. P., Anasori, B. *et al.* Oxidation Stability of Colloidal Two-Dimensional Titanium Carbides (MXenes). *Chem. Mater.* **29**, 4848-4856, doi:10.1021/acs.chemmater.7b00745 (2017).

49 Zhao, X., Vashisth, A., Prehn, E., Sun, W., Shah, S. A. *et al.* Antioxidants Unlock Shelf-Stable Ti3C2Tx (MXene) Nanosheet Dispersions. *Matter* **1**, 513-526, doi:https://doi.org/10.1016/j.matt.2019.05.020.

50 Natu, V., Sokol, M., Verger, L. & Barsoum, M. W. Effect of Edge Charges on Stability and Aggregation of Ti3C2Tz MXene Colloidal Suspensions. *J. Phys. Chem. C* **122**, 27745-27753, doi:10.1021/acs.jpcc.8b08860 (2018).

51 Natu, V., Clites, M., Pomerantseva, E. & Barsoum, M. W. Mesoporous MXene powders synthesized by acid induced crumpling and their use as Na-ion battery anodes. *Mater. Res. Lett.* **6**, 230-235, doi:10.1080/21663831.2018.1434249 (2018).

52 Zhao, D., Clites, M., Ying, G., Kota, S., Wang, J. *et al.* Alkali-induced crumpling of Ti3C2Tx (MXene) to form 3D porous networks for sodium ion storage. *Chem. Commun.* **54**, 4533-4536, doi:10.1039/C8CC00649K (2018).

53 Wei, Z., Peigen, Z., Wubian, T., Xia, Q., Yamei, Z. *et al.* Alkali treated Ti3C2Tx MXenes and their dye adsorption performance. *Mater. Chem. Phys.* **206**, 270-276, doi:https://doi.org/10.1016/j.matchemphys.2017.12.034 (2018).

54 Loh, K. J., Kim, J., Lynch, J. P., Kam, N. W. S. & Kotov, N. A. Multifunctional layer-by-layer carbon nanotube–polyelectrolyte thin films for strain and corrosion sensing. *Smart Mater. Struct.* **16**, 429 (2007).

55 Shaibani, P. M., Etayash, H., Naicker, S., Kaur, K. & Thundat, T. Metabolic Study of Cancer Cells Using a pH Sensitive Hydrogel Nanofiber Light

Addressable Potentiometric Sensor. *ACS Sensors* **2**, 151-156, doi:10.1021/acssensors.6b00632 (2017).

56 Ang, P. K., Chen, W., Wee, A. T. S. & Loh, K. P. Solution-Gated Epitaxial Graphene as pH Sensor. *JACS* **130**, 14392-14393, doi:10.1021/ja805090z (2008).

57 Lakard, B., Segut, O., Lakard, S., Herlem, G. & Gharbi, T. Potentiometric miniaturized pH sensors based on polypyrrole films. *Sensors Actuators B: Chem.* **122**, 101-108, doi:https://doi.org/10.1016/j.snb.2006.04.112 (2007).

58 Lee, C., Akbar, S. A. & Park, C. O. Potentiometric CO2 gas sensor with lithium phosphorous oxynitride electrolyte. *Sensors Actuators B: Chem.* **80**, 234-242, doi:https://doi.org/10.1016/S0925-4005(01)00902-9 (2001).

59 Pan, T.-M., Wang, C.-W., Mondal, S. & Pang, S.-T. Super-Nernstian sensitivity in microfabricated electrochemical pH sensor based on CeTixOy film for biofluid monitoring. *Electrochim. Acta* **261**, 482-490, doi:https://doi.org/10.1016/j.electacta.2017.12.163 (2018).

60 Terci, D. B. L. & Rossi, A. V. Natural pH indicators: Using paper or solution? *Quim. Nova* **25**, 684-688, doi:10.1590/s0100-40422002000400026 (2002).

61 Paek, K., Yang, H., Lee, J., Park, J. & Kim, B. J. Efficient Colorimetric pH Sensor Based on Responsive Polymer–Quantum Dot Integrated Graphene Oxide. *ACS Nano* **8**, 2848-2856, doi:10.1021/nn406657b (2014).

62 Qin, Y., Kwon, H.-J., Howlader, M. M. R. & Deen, M. J. Microfabricated electrochemical pH and free chlorine sensors for water quality monitoring: recent

advances and research challenges. *RSC Adv.* **5**, 69086-69109, doi:10.1039/C5RA11291E (2015).

63 Lei, N., Li, P., Xue, W. & Xu, J. Simple graphene chemiresistors as pH sensors: fabrication and characterization. *Meas. Sci. Technol.* **22**, 107002, doi:10.1088/0957-0233/22/10/107002 (2011).

64 An, H., Habib, T., Shah, S., Gao, H., Radovic, M. *et al.* Surface-agnostic highly stretchable and bendable conductive MXene multilayers. *Sci. Adv.* **4**, doi:10.1126/sciadv.aaq0118 (2018).

65 Cai, Y., Shen, J., Ge, G., Zhang, Y., Jin, W. *et al.* Stretchable Ti3C2Tx MXene/Carbon Nanotube Composite Based Strain Sensor with Ultrahigh Sensitivity and Tunable Sensing Range. *ACS Nano* **12**, 56-62, doi:10.1021/acsnano.7b06251 (2018).

66 Yuan, W., Yang, K., Peng, H., Li, F. & Yin, F. A flexible VOCs sensor based on a 3D Mxene framework with a high sensing performance. *J. Mater. Chem. A* **6**, 18116-18124, doi:10.1039/C8TA06928J (2018).

67 Koh, H.-J., Kim, S. J., Maleski, K., Cho, S.-Y., Kim, Y.-J. *et al.* Enhanced Selectivity of MXene Gas Sensors through Metal Ion Intercalation: In Situ X-ray Diffraction Study. *ACS Sensors* **4**, 1365-1372, doi:10.1021/acssensors.9b00310 (2019).

68 Lee, E., VahidMohammadi, A., Prorok, B. C., Yoon, Y. S., Beidaghi, M. *et al.* Room Temperature Gas Sensing of Two-Dimensional Titanium Carbide

(MXene). *ACS Appl. Mater. Interfaces* **9**, 37184-37190, doi:10.1021/acsami.7b11055 (2017).

69 Salvo, P., Melai, B., Calisi, N., Paoletti, C., Bellagambi, F. *et al.* Graphene-based devices for measuring pH. *Sensors Actuators B: Chem.* **256**, 976-991, doi:https://doi.org/10.1016/j.snb.2017.10.037 (2018).

70 Nernst, W. in *ZPC* Vol. 4U 129 (1889).

71 Buck, R. P., Rondinini, S., Covington, A. K., Baucke, F. G. K., Brett Christopher, M. A. *et al.* in *Pure Appl. Chem.* Vol. 74 2169 (2002).

72 Das, A., Ko, D. H., Chen, C.-H., Chang, L.-B., Lai, C.-S. *et al.* Highly sensitive palladium oxide thin film extended gate FETs as pH sensor. *Sensors Actuators B: Chem.* **205**, 199-205, doi:https://doi.org/10.1016/j.snb.2014.08.057 (2014).

73 Santos, L., Neto, J. P., Crespo, A., Nunes, D., Costa, N. *et al.* WO3 Nanoparticle-Based Conformable pH Sensor. *ACS Appl. Mater. Interfaces* **6**, 12226-12234, doi:10.1021/am501724h (2014).

74 Nyein, H. Y. Y., Gao, W., Shahpar, Z., Emaminejad, S., Challa, S. *et al.* A Wearable Electrochemical Platform for Noninvasive Simultaneous Monitoring of Ca2+ and pH. *ACS Nano* **10**, 7216-7224, doi:10.1021/acsnano.6b04005 (2016).

75 Yin, M., Gu, B., Zhao, Q., Qian, J., Zhang, A. *et al.* Highly sensitive and fast responsive fiber-optic modal interferometric pH sensor based on polyelectrolyte complex and polyelectrolyte self-assembled nanocoating. *Anal. Bioanal. Chem.* **399**, 3623-3631, doi:10.1007/s00216-011-4705-0 (2011).

76 Goicoechea, J., Zamarreño, C. R., Matías, I. R. & Arregui, F. J. Optical fiber pH sensors based on layer-by-layer electrostatic self-assembled Neutral Red. *Sensors Actuators B: Chem.* **132**, 305-311, doi:https://doi.org/10.1016/j.snb.2008.01.056 (2008).

77 Loh, K. J., Lynch, J. P. & Kotov, N. A. *Passive wireless strain and pH sensing using carbon nanotube-gold nanocomposite thin films*. Vol. 6529 SS (SPIE, 2007).

78 Lei, K. F., Lee, K.-F. & Yang, S.-I. Fabrication of carbon nanotube-based pH sensor for paper-based microfluidics. *Microelectron. Eng.* **100**, 1-5, doi:https://doi.org/10.1016/j.mee.2012.07.113 (2012).

79 Nguyen, H. D., Nguyen, T. H., Hoang, N. V., Le, N. N., Nguyen, T. N. N. *et al.* pH sensitivity of emeraldine salt polyaniline and poly(vinyl butyral) blend. *Advances in Natural Sciences: Nanoscience and Nanotechnology* **5**, 045001, doi:10.1088/2043-6262/5/4/045001 (2014).

80 Lee, Y. T., Lee, E., Lee, J. M. & Lee, W. Micro-sized pH sensors based on patterned Pd structures using an electrolysis method. *CAP* **9**, e218-e221, doi:https://doi.org/10.1016/j.cap.2009.06.022 (2009).

81 Jung, D., Han, M.-E. & Lee, G. S. pH-sensing characteristics of multi-walled carbon nanotube sheet. *Mater. Lett.* **116**, 57-60, doi:https://doi.org/10.1016/j.matlet.2013.10.095 (2014).

82 De, S. & Lutkenhaus, J. L. Corrosion behaviour of eco-friendly airbrushed reduced graphene oxide-poly(vinyl alcohol) coatings. *Green Chem.* **20**, 506-514, doi:10.1039/C7GC02882B (2018).

83 Weng, G.-M., Li, J., Alhabeb, M., Karpovich, C., Wang, H. *et al.* Layer-by-Layer Assembly of Cross-Functional Semi-transparent MXene-Carbon Nanotubes Composite Films for Next-Generation Electromagnetic Interference Shielding. *Adv. Funct. Mater.* **28**, 1803360, doi:10.1002/adfm.201803360 (2018).

84 Mutyala, S. & Mathiyarasu, J. A reagentless non-enzymatic hydrogen peroxide sensor presented using electrochemically reduced graphene oxide modified glassy carbon electrode. *Materials Science and Engineering: C* **69**, 398-406, doi:https://doi.org/10.1016/j.msec.2016.06.069 (2016).

85 Guo, S., Wen, D., Zhai, Y., Dong, S. & Wang, E. Platinum Nanoparticle Ensemble-on-Graphene Hybrid Nanosheet: One-Pot, Rapid Synthesis, and Used as New Electrode Material for Electrochemical Sensing. *ACS Nano* **4**, 3959-3968, doi:10.1021/nn100852h (2010).

86 Kang, X., Mai, Z., Zou, X., Cai, P. & Mo, J. A sensitive nonenzymatic glucose sensor in alkaline media with a copper nanocluster/multiwall carbon nanotube-modified glassy carbon electrode. *Anal Biochem* **363**, 143-150, doi:https://doi.org/10.1016/j.ab.2007.01.003 (2007).

87 Kang, X., Wang, J., Wu, H., Liu, J., Aksay, I. A. *et al.* A graphene-based electrochemical sensor for sensitive detection of paracetamol. *Talanta* **81**, 754-759, doi:https://doi.org/10.1016/j.talanta.2010.01.009 (2010).

88 Sukhorukov, G. B., Donath, E., Lichtenfeld, H., Knippel, E., Knippel, M. *et al.* Layer-by-layer self assembly of polyelectrolytes on colloidal particles. *Colloids Surf. Physicochem. Eng. Aspects* **137**, 253-266, doi:https://doi.org/10.1016/S0927-7757(98)00213-1 (1998).

89 Kovtyukhova, N. I., Ollivier, P. J., Martin, B. R., Mallouk, T. E., Chizhik, S. A. *et al.* Layer-by-Layer Assembly of Ultrathin Composite Films from Micron-Sized Graphite Oxide Sheets and Polycations. *Chem. Mater.* **11**, 771-778, doi:10.1021/cm981085u (1999).

90 Lvov, Y., Ariga, K., Ichinose, I. & Kunitake, T. Assembly of Multicomponent Protein Films by Means of Electrostatic Layer-by-Layer Adsorption. *JACS* **117**, 6117-6123, doi:10.1021/ja00127a026 (1995).

91 Wilson, J. T., Cui, W. & Chaikof, E. L. Layer-by-Layer Assembly of a Conformal Nanothin PEG Coating for Intraportal Islet Transplantation. *Nano Lett.* **8**, 1940-1948, doi:10.1021/nl080694q (2008).

92 Díez-Pascual, A. & Shuttleworth, P. Layer-by-Layer Assembly of Biopolyelectrolytes onto Thermo/pH-Responsive Micro/Nano-Gels. *Materials* **7**, 7472 (2014).

93 Zhang, H., Wang, C., Zhu, G. & Zacharia, N. S. Self-Healing of Bulk Polyelectrolyte Complex Material as a Function of pH and Salt. *ACS Appl. Mater. Interfaces* **8**, 26258-26265, doi:10.1021/acsami.6b06776 (2016).

94 Hummers, W. S. & Offeman, R. E. Preparation of Graphitic Oxide. *JACS* **80**, 1339-1339, doi:10.1021/ja01539a017 (1958).

95 Zhao, M.-Q., Trainor, N., Ren, C. E., Torelli, M., Anasori, B. *et al.* Scalable Manufacturing of Large and Flexible Sheets of MXene/Graphene Heterostructures. *Adv. Mater. Technol.* **0**, 1800639, doi:10.1002/admt.201800639.

96 Rodahl, M. & Kasemo, B. On the measurement of thin liquid overlayers with the quartz-crystal microbalance. *Sensors and Actuators A: Physical* **54**, 448-456, doi:https://doi.org/10.1016/S0924-4247(97)80002-7 (1996).

97 Sauerbrey, G. Verwendung von Schwingquarzen zur Wägung dünner Schichten und zur Mikrowägung. *ZPhy* **155**, 206-222, doi:10.1007/bf01337937 (1959).

98 Shah, S. A., Habib, T., Gao, H., Gao, P., Sun, W. *et al.* Template-free 3D titanium carbide (Ti3C2Tx) MXene particles crumpled by capillary forces. *Chem. Commun.* **53**, 400-403, doi:10.1039/C6CC07733A (2017).

99 Wong, J. E., Rehfeldt, F., Hänni, P., Tanaka, M. & Klitzing, R. v. Swelling Behavior of Polyelectrolyte Multilayers in Saturated Water Vapor. *Macromolecules* **37**, 7285-7289, doi:10.1021/ma0351930 (2004).

100 Gu, Y., Weinheimer, E. K., Ji, X., Wiener, C. G. & Zacharia, N. S. Response of Swelling Behavior of Weak Branched Poly(ethylene imine)/Poly(acrylic acid)

Polyelectrolyte Multilayers to Thermal Treatment. *Langmuir* **32**, 6020-6027, doi:10.1021/acs.langmuir.6b00206 (2016).

101 Pan, H., Marsh, J. N., Christenson, E. T., Soman, N. R., Ivashyna, O. *et al.* in *Methods Enzymol.* Vol. 508 (ed Nejat Düzgüneş) 17-39 (Academic Press, 2012).

102 Zheng, S., Tu, Q., Urban, J. J., Li, S. & Mi, B. Swelling of Graphene Oxide Membranes in Aqueous Solution: Characterization of Interlayer Spacing and Insight into Water Transport Mechanisms. *ACS Nano* **11**, 6440-6450, doi:10.1021/acsnano.7b02999 (2017).

103 Li, N., Jiang, Y., Zhou, C., Xiao, Y., Meng, B. *et al.* High-Performance Humidity Sensor Based on Urchin-Like Composite of Ti3C2 MXene-Derived TiO2 Nanowires. *ACS Appl. Mater. Interfaces*, doi:10.1021/acsami.9b12168 (2019).

104 Zhang, W., Zhao, Q. & Yuan, J. Porous Polyelectrolytes: The Interplay of Charge and Pores for New Functionalities. *Angew. Chem. Int. Ed.* **57**, 6754-6773, doi:10.1002/anie.201710272 (2018).